



**STRUCTURAL SYSTEMS  
RESEARCH PROJECT**

Report No.  
SSRP 18-03

**Interaction of MSE Abutments with Bridge  
Superstructures under Seismic Loading  
– Numerical Simulations**

by

**Yewei Zheng**

**John S. McCartney**

**P. Benson Shing**

**Patrick J. Fox**

Final Report.

June 2018

Department of Structural Engineering  
University of California, San Diego  
La Jolla, California 92093-0085

1. Report No. SSRP 18-03		2. Government Accession No.		3. Recipient's Catalog No.	
4. Title and Subtitle  Interaction of MSE Abutments with Bridge Superstructures under Seismic Loading – Numerical Simulations				5. Report Date  06/2018	
				6. Performing Organization Code	
7. Author(s)  Yewei Zheng, John S. McCartney, P. Benson Shing, and Patrick J. Fox				8. Performing Organization Report No.  UCSD/SSRP 18-03	
9. Performing Organization Name and Address  Division of Structural Engineering School of Engineering University of California, San Diego La Jolla, California 92093-0085				10. Work Unit No. (TRAIS)	
				11. Contract or Grant No.  TPF-5(276)	
12. Sponsoring Agency Name and Address  Washington Department of Transportation 310 Maple Park Avenue SE P.O. Box 47300 Olympia, WA 98504-7300				13. Type of Report and Period Covered  Final Report	
				14. Sponsoring Agency Code	
15. Supplementary Notes Prepared in cooperation with the State of California Department of Transportation and the Washington Department of Transportation through the FHWA Transportation Pooled Fund project TPF-5(276). This final report is a companion to an earlier report entitled "Interaction of MSE Abutments with Bridge Superstructures under Seismic Loading – Shaking Table Testing"					
16. Abstract This report presents results from numerical simulations on mechanically-stabilized earth (MSE) bridge abutments under dynamic loading. A hysteretic soil model was used to simulate the reduction of secant modulus of the backfill soil with increasing shear strain. The hysteretic soil model parameters were calibrated according to modulus reduction curves and damping curves calculated using empirical relationships from published literature. Numerical simulations were first conducted to simulate the response of the shaking table tests on half-scale MSE bridge abutments performed as part of this study. Results indicate that the numerical model could capture the effects of reinforcement spacing, reinforcement stiffness, and bridge surcharge stress on facing displacements and bridge seat settlements under dynamic loading. Simulated residual facing displacements were slightly overestimated, whereas the simulated residual bridge seat settlements were in good agreement with the measured values. A parametric study was then performed using the validated numerical model for full-scale MSE bridge abutments. The results from the parametric study indicate that facing displacements and abutment compressions for MSE bridge abutments increase significantly with increasing reinforcement vertical spacing and decreasing reinforcement stiffness under dynamic loading. Bridge surcharge stress also has significant effects on the seismic response due to combined effect of change in soil stiffness and inertial forces during shaking.					
17. Key Words  Mechanically stabilized earth, bridge abutments, seismic response, numerical simulation, geogrids				18. Distribution Statement  Unlimited	
19. Security Classification (of this report)  Unclassified		20. Security Classification (of this page)  Unclassified		21. No. of Pages  65	22. Price

University of California, San Diego  
Department of Structural Engineering  
Structural Systems Research Project

Report No. SSRP 18-03

# **Interaction of MSE Abutments with Bridge Superstructures under Seismic Loading – Numerical Simulations**

by

**Yewei Zheng, Ph.D.**

*Postdoctoral Research Scholar*

**John S. McCartney, Ph.D., P.E.**

*Associate Professor*

**P. Benson Shing, Ph.D.**

*Professor and Chair*

**Patrick J. Fox, Ph.D., P.E.**

*Shaw Professor and Department Head*

Final Report submitted to the California Department of Transportation  
under Contact No. 65A0556 and to Washington Department of Transportation under Federal  
Highway Administration Transportation Pooled Fund Project No. TPF-5(276).

Department of Structural Engineering  
University of California, San Diego  
La Jolla, California 92093-0085

June 2018

## **DISCLAIMER**

This document is disseminated in the interest of information exchange. The contents of this report reflect the views of the authors who are responsible for the facts and accuracy of the data presented herein. The contents do not necessarily reflect the official views or policies of the State of California or the Federal Highway Administration. This publication does not constitute a standard, specification or regulation. This report does not constitute an endorsement by the California Department of Transportation of any product described herein.

For individuals with sensory disabilities, this document is available in Braille, large print, audiocassette, or compact disk. To obtain a copy of this document in one of these alternate formats, please contact: the Division of Research and Innovation, MS-83, California Department of Transportation, P.O. Box 942873, Sacramento, CA 94273-0001.

## **ACKNOWLEDGEMENTS**

Financial support for this study provided by the California Department of Transportation (Caltrans) Project 65A0556 and Washington Department of Transportation through the Federal Highway Administration (FHWA) Transportation Pooled Fund Project TPF-5(276) with partner states CA, ID, MS, UT, WA is gratefully acknowledged. The authors thank Charles Sikorsky of Caltrans and Lu Saechao of Washington DOT for their supervision of these projects, respectively.

## ABSTRACT

This report presents results from numerical simulations on mechanically-stabilized earth (MSE) bridge abutments under dynamic loading. A hysteretic soil model was used to simulate the reduction of secant modulus of the backfill soil with increasing shear strain. The hysteretic soil model parameters were calibrated according to modulus reduction curves and damping curves calculated using empirical relationships from published literature. Numerical simulations were first conducted to simulate the response of the shaking table tests on half-scale MSE bridge abutments performed as part of this study. Results indicate that the numerical model could capture the effects of reinforcement spacing, reinforcement stiffness, and bridge surcharge stress on facing displacements and bridge seat settlements under dynamic loading. Simulated residual facing displacements were slightly overestimated, whereas the simulated residual bridge seat settlements were in good agreement with the measured values. A parametric study was then performed using the validated numerical model for full-scale MSE bridge abutments. The results from the parametric study indicate that facing displacements and abutment compressions for MSE bridge abutments increase significantly with increasing reinforcement vertical spacing and decreasing reinforcement stiffness under dynamic loading. Bridge surcharge stress also has significant effects on the seismic response due to combined effect of change in soil stiffness and inertial forces during shaking.

# Table of Contents

<b>Chapter 1</b>	<b>Introduction</b>	1
<b>Chapter 2</b>	<b>Literature Review</b>	5
2.1	Static Response	5
2.2	Dynamic Response	10
2.3	Summary	13
<b>Chapter 3</b>	<b>Numerical Simulation of Shaking Table Tests on MSE Bridge Abutments</b>	14
3.1	Introduction	14
3.2	Model Geometry	15
3.3	Material Model and Properties	16
3.3.1	<i>Soils</i>	16
3.3.2	<i>Reinforcements</i>	22
3.3.3	<i>Structural Components</i>	22
3.3.4	<i>Interfaces</i>	22
3.4	Static Modeling Procedures	23
3.5	Dynamic Modeling Procedures	23
3.6	Simulation Results	24
3.6.1	<i>Facing Displacements</i>	24
3.6.2	<i>Bridge Seat and Bridge Beam Displacements</i>	27
3.6.3	<i>Accelerations</i>	28
3.6.4	<i>Vertical and Lateral Stresses</i>	31
3.6.5	<i>Reinforcement Strains</i>	33
<b>Chapter 4</b>	<b>Parametric Study of MSE Bridge Abutments under Dynamic Loading</b>	36
4.1	Baseline Case	36
4.1.1	<i>Numerical Model</i>	36
4.1.2	<i>Simulation Results</i>	39
4.2	Reinforcement Spacing	41
4.3	Reinforcement Stiffness	43
4.4	Secondary Reinforcement	44
4.5	Bridge Surcharge Stress	46
4.6	Bridge Seat Setback Distance	48
4.7	Bearing Pad Friction Coefficient	49
4.8	Earthquake Motion	50

<b>Chapter 5</b>	<b>Conclusions and Recommendations</b> .....	52
5.1	Conclusions.....	52
5.2	Recommendations.....	53
<b>References</b>	.....	54

## Chapter 1 Introduction

Reinforced soil walls have been extensively used in transportation infrastructure because they provides many advantages over traditional gravity- or cantilever-type retaining walls, including lower cost, faster and easier construction, and acceptable deformation performance under static and seismic loading conditions (Berg et al. 2009). Two design philosophies for using reinforced soil walls have been adopted by the US Federal Highway Administration (FHWA), mechanically-stabilized earth (MSE) walls and geosynthetic reinforced soil (GRS) walls. The design philosophy for MSE walls is described in detail in FHWA-NHI-10-024 (Berg et al. 2009). MSE walls involve either inextensible metallic reinforcements or extensible geosynthetic reinforcements embedded in compacted granular soil, and the reinforcement spacing and length is determined in design by assuming that they are tie-back anchors. The design philosophy for GRS walls is described in detail in FHWA-HRT-11-026 (Adams et al. 2011a). GRS walls involve closely-spaced geosynthetic reinforcements (spacing  $\leq 0.3$  m) embedded in compacted granular soil to form a GRS composite structure. Despite the difference in design philosophies for MSE and GRS walls, many technical papers use these acronyms interchangeably when describing retaining walls and bridge abutments reinforced with geosynthetics. In the literature review for this report, the term “GRS” is used when discussing geosynthetic reinforced soil structures in general, even when they may not have been designed following the reinforcement spacing requirement in the GRS design philosophy described by Adams et al. (2011a).

In recent years, MSE walls have been used as bridge abutments where the bridge beam load is applied as a surcharge to the top of a reinforced soil mass via a shallow footing. This concept offers significant cost and construction time savings in comparison to traditional pile-supported bridge abutment designs and can reduce differential settlements between the bridge and approach roadways (Abu-Hejleh et al. 2002). The Earth Retaining Systems, Substructures, Loads, and General Earthquake Committees of Caltrans released a joint position paper on MSE bridge abutments (Caltrans 2017). In the joint position paper, MSE walls were approved for use in Type 1 and Type 2 MSE bridge abutments, which are shown in Figure 1.1 and Figure 1.2, respectively. The bridge beam load is supported by a footing resting on the MSE wall for the Type 1 MSE bridge abutment, whereas the bridge beam load is supported on a footing resting on piles for the Type 2 MSE bridge abutment. Even though the Type 1 and Type 2 MSE bridge abutments have been approved for use by Caltrans, their response under seismic loading is uncertain and further refinements may be needed for their design. In addition, the FHWA has developed a newer bridge abutment design called the geosynthetic reinforced soil-integrated bridge system (GRS-IBS) shown in Figure 1.3 in which the bridge superstructure and the approach fill are more integrated, with the bridge beam resting directly on the reinforced soil mass (Adams et al. 2011a). However, this GRS-IBS abutment has not been approved for use by Caltrans (Caltrans 2017). Therefore, this study only focuses on understanding the seismic response of Type 1 MSE bridge abutments.

Many studies have shown that the MSE and GRS bridge abutments have acceptable deformations under service load conditions. For example, Lee and Wu (2004) reviewed several case studies of in-service GRS bridge abutments (Won et al. 1996; Abu-Hejleh et al. 2002), and reported generally satisfactory performance in terms of lateral facing displacements and bridge seat settlements under service load conditions. Several case histories for in-service geosynthetic reinforced soil-integrated bridge system (GRS-IBS) abutments also have been reported, and each show good field performance regarding bridge settlement, abutment compression, and differential settlement (Adams et al. 2007, 2008, 2011b; Warren et al. 2010; Budge et al. 2014; Saghebfar et al. 2017).

A concern regarding the use of MSE bridge abutments is that the magnitude of vertical settlements of the backfill during a major earthquake is uncertain, and research is needed to clarify if the magnitude of these vertical settlements may be large enough to impose unacceptable stresses in a multi-span bridge beam with internal (column) supports. Associated facing displacements of the MSE bridge abutment due to seismic loading are also a potential concern. Thus, while MSE bridge abutment technology offers substantial cost- and time-savings for construction, there are concerns regarding the use of this technology in high seismic areas and little information is available to guide designers on how to improve the seismic response of these structures. Yen et al. (2011) conducted post-earthquake reconnaissance for the 2010 Maule Earthquake, and found that a MSE bridge abutment exhibited no signs of lateral or vertical displacements after shaking. However, the bridge suffered minor damage that may have resulted from the severe bridge skew angle. Shaking table tests conducted by Helwany et al. (2012) on a 3.6 m-high GRS bridge abutment indicated no significant distress during shaking with horizontal accelerations up to 1g. Due to the limited information on the seismic performance of MSE bridge abutments in the field and in previous shaking table tests, more experimental evaluations and numerical simulations are needed to understand the potential issues and for impacts of different design variables on the performance characteristics of MSE bridge abutments under dynamic loading.

The overall purpose of this project was to investigate the dynamic response of MSE bridge abutments through physical testing and numerical modeling. A separate report by McCartney et al. (2018) presented results and analysis from a total of six shaking table tests on half-scale MSE bridge abutments with various configurations and loading conditions. This report focuses on the numerical simulations of MSE bridge abutments (i.e., Type 1 MSE bridge abutment design in Figure 1.1) for shaking in the longitudinal direction. The specific objectives of this report are to develop a numerical model for dynamic analysis of MSE bridge abutments and to understand the effects of different design variables on the dynamic response of MSE bridge abutments. This report presents validation of a numerical model for MSE bridge abutments under dynamic loading using data from shaking table tests (McCartney et al. 2018) and a parametric study to investigate the effects of various design parameters on the facing displacements and abutment compressions due to earthquake motions.

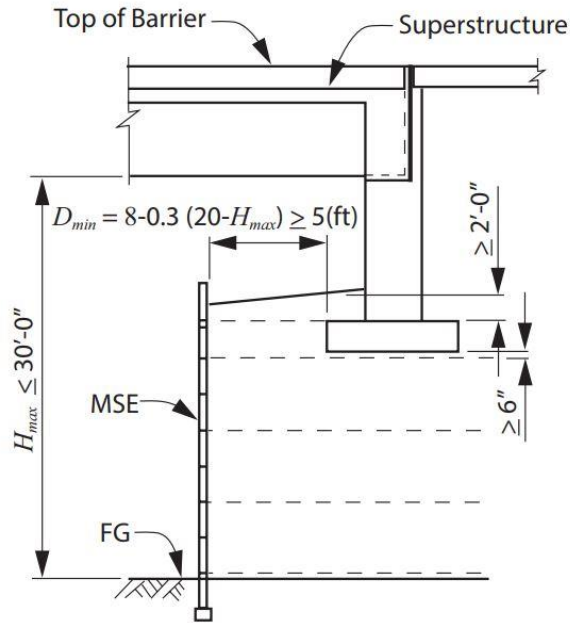


Figure 1.1 Typical geometry for Type 1 MSE bridge abutment (Caltrans 2017).

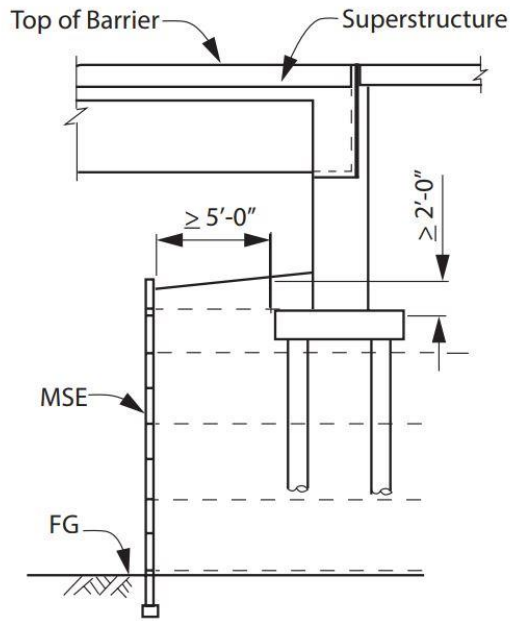


Figure 1.2 Typical geometry for Type 2 MSE bridge abutment (Caltrans 2017).

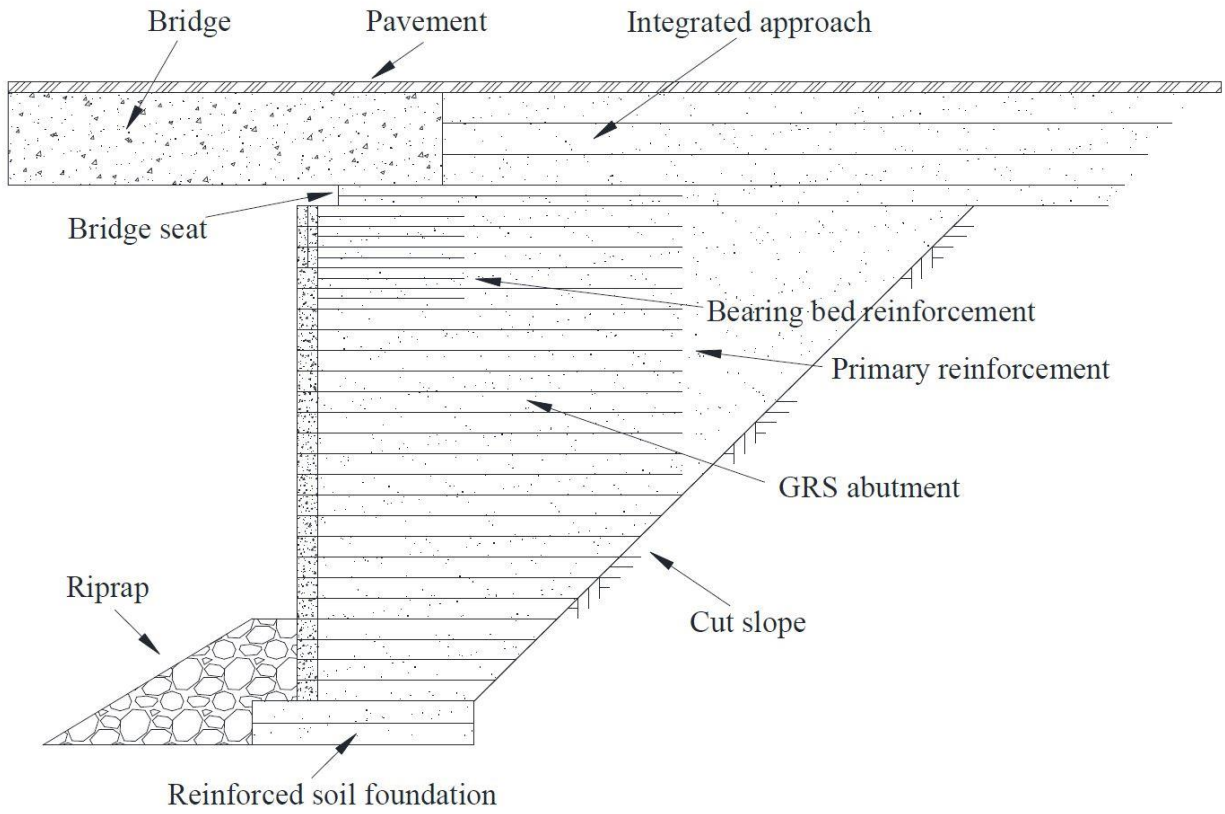


Figure 1.3 Typical geometry for GRS-IBS bridge abutment (after Adams et al. 2011a).

## Chapter 2 Literature Review

### 2.1 Static Response

Bathurst et al. (1992) and Karpurapu and Bathurst (1995) simulated two full-scale GRS walls with incremental panel facing and full height panel facing using the finite element program GEOFEM. A modified hyperbolic model that included dilation was used to simulate the backfill soil, and the reinforcement was simulated with a nonlinear load-strain model using uniaxial elements. Zero thickness joint elements with Mohr-Coulomb failure criterion were used to simulate the interfaces between soil and reinforcement, and between soil and facing panels. Triaxial tests and direct shear tests were conducted to determine parameters for the modified Duncan-Chang hyperbolic model. Constant creep load tests were carried out to obtain the isochronous load-strain-time relationships for the reinforcement, and interface shear tests were conducted to determine shear stiffness of various interfaces. Simulation results, including lateral facing displacements and reinforcement strains at the end of construction and under uniform surcharge loading, were compared with experimental results, and showed good agreement for both working stress and collapse conditions. It is important to consider the soil dilation to accurately simulate the performance of GRS walls because soil dilation have an important effect on transferring load from reinforcement to soils during shearing. Lateral facing displacements and reinforcement strains could be over-predicted by a factor of two if soil dilation was not accounted for. The simulated failure surface was also in good agreement with experimental observed failure surface and the failure surface predicted using Rankine earth pressure theory.

Ho and Rowe (1996) and Rowe and Ho (1997, 1998) performed parametric studies on GRS walls with continuous facing panels using the finite element program AFENA. In these studies, the effects of reinforcement properties, soil properties, interface friction angles, wall facing rigidity, and wall height were investigated. The backfill soil was modeled as an elasto-plastic material with the Mohr-Coulomb failure criterion and non-associated flow rule. The reinforcement was modeled using linearly elastic bar elements with negligible compressive strength. Soil-reinforcement, soil-facing panel, and soil-foundation interfaces were modeled using joint elements with the Mohr-Coulomb failure criterion and zero dilation. Simulation results indicated that reinforcement stiffness and backfill soil friction angle have the most significant effects on the lateral facing displacements, whereas the interface friction angles, soil Young's modulus, and facing rigidity are less important. For a reinforcement length to wall height ratio ( $L/H$ ) greater than 0.7, the effect of reinforcement length on the lateral facing displacements and reinforcement strains was very small, while the effect could be significant for  $L/H$  less than 0.7. The maximum reinforcement load increases with increasing reinforcement stiffness density, decreasing backfill soil friction angle, decreasing soil-facing interface friction angle, and decreasing facing rigidity.

Helwany et al. (1999) verified a finite element model using measured results from the Denver Test Wall using the finite element program DACSAR. In this study, the backfill soil was simulated

using a nonlinear elastic hyperbolic model, and the model parameters were calibrated from triaxial tests. The timber facing and geotextile reinforcement were modeled using linearly elastic beam elements and truss elements, respectively. Simulated lateral facing displacements and reinforcement strains were in reasonable agreement with measured results. A parametric study was conducted using the validated numerical model to investigate the effects of various factors on the behavior of GRS wall under a uniform surcharge stress of 35 kPa. Results indicated that the backfill soil type was the most important factor that affected the performance of GRS walls. Reinforcement stiffness was also important when the backfill soil stiffness and strength were low. Design charts were developed for selecting appropriate backfill soil type and reinforcement stiffness to satisfy the performance requirements (e.g. maximum lateral facing displacement, maximum reinforcement strain, and/or average factor of safety) for the design of GRS walls.

Ling et al. (2000) used the finite element program M-CANDE to reproduce results of a full-scale GRS retaining wall model test at the Public Works Research Institute (referred to as PWRI Wall). The PWRI Wall was 6 m-high and 5 m-wide, and was reinforced using primary geogrid (3.5 m-long) and secondary geogrid (1.0 m-long). In this study, both the backfill soil and geosynthetic reinforcement were modeled using the hyperbolic model, and the model parameters were calibrated using results from triaxial tests for the backfill soil and tensile tests for the reinforcement. The block-block interface and soil-block interfaces were simulated using interface elements, and the interface friction angles and tensile strengths were determined from interface direct shear tests. Simulated results, including lateral facing displacements, lateral and vertical stresses, and reinforcement strains during construction were compared with measured results, and showed satisfactory agreement. Ling and Leshchinsky (2003) carried out a parametric study using the validated model to investigate the effects of various design parameters on the behavior of GRS walls under working stress conditions. Results indicated that lateral facing displacements and maximum reinforcement tensile forces increased with increasing reinforcement vertical spacing. Lateral facing displacements decreased with increasing reinforcement stiffness, whereas the maximum tensile forces were the largest for the stiffest reinforcement. For block-block interface friction angles greater than 20 °, the variations for wall displacements and maximum reinforcement strains were negligible. Ling (2003) also compared simplistic and sophisticated finite element analyses for GRS walls. Both the backfill soil and geosynthetic reinforcement were characterized using hyperbolic model in the simplistic analysis, whereas in the sophisticated analysis, the backfill soil was modeled using a generalized plasticity model and the geogrid was simulated using a bounding surface model. Results for wall facing displacements, lateral and vertical stresses, and reinforcement strains from simplistic and sophisticated analyses were in good agreement, and both provided a reasonable match with measured results from a full-scale model test.

Lee (2000) validated a FLAC model with monitored results from several instrumented full-scale GRS walls. A parametric study was carried out to investigate the influences of soil properties, reinforcement properties, toe restraint, and facing type on the performance of GRS retaining walls.

Results indicated that the backfill soil strength properties and global reinforcement spacing have the most significant effects on the facing displacements and reinforcement strains. Toe restraint (embedded toe condition) could reduce the maximum facing displacement and reinforcement tensile forces. For GRS walls constructed using good quality backfill soil and with large reinforcement vertical spacing, secondary reinforcement was effective on improving the performance. A structural facing system such as modular blocks and concrete panels could increase the stability, and reduce wall deformations and reinforcement strains, especially for GRS walls with large reinforcement spacing.

Leshchinsky and Vulova (2001) investigated the effects of reinforcement spacing on the failure mechanisms of GRS walls using FLAC. The backfill soil was modeled using the Duncan-Chang hyperbolic stress-strain relationship prior to failure and the Mohr-Coulomb failure criterion. The frictional connection between the reinforcement and facing blocks was simulated using beam elements and interface elements. Four modes of failure were observed, including external (direct sliding and toppling), deep seated (bearing capacity), compound, and connection, based on the development of plastic zones. Deep seated failure occurred for the cases with closely-spaced reinforcement and weak foundation soil. Connection failures were observed for all cases with reinforcement spacing equal to or greater than 0.6 m. Leshchinsky and Vulova (2001) suggested that reinforcement spacing plays an important role in the behavior of GRS walls and significantly affects the potential failure mode.

Hatami and Bathurst (2005a; b) validated a FLAC model using measured results from full-scale model tests on GRS walls at the end of construction. The backfill soil was modeled as a nonlinear elastic-plastic material with the Duncan-Chang hyperbolic relationship, Mohr-Coulomb failure criterion and non-associated flow rule. The reinforcement was also simulated using a hyperbolic model, and was assumed to be rigidly connected to the facing blocks using beam elements. In this study, the backfill soil compaction during construction were simulated using a temporarily-applied surcharge stress of 8 kPa after placement of each lift, and was removed before the placement of the next soil lift. Simulated results, including toe loads, vertical foundation pressures, facing displacements, connection loads, and reinforcement strains were compared with measured results, and yielded good agreement. The influence of soil constitutive model on the wall performance was also investigated. Simulation results for a linearly elastic-perfectly plastic soil model showed good agreement with regarding to facing displacements and toe loads, but lesser agreement for reinforcement strain distributions. Hatami and Bathurst (2005c) and Bathurst and Hatami (2006a) investigated the effects of various design parameters on the behavior of GRS walls at the end of construction using FLAC. Results showed that, as the wall height increased, the maximum lateral facing displacement increased. For a granular soil, a value of cohesion as low as 10 kPa can significantly reduce lateral facing displacements and can also influence the facing displacement pattern and reinforcement strain distribution. Hatami and Bathurst (2006) and Bathurst and Hatami (2006b) further validated the FLAC model for GRS retaining walls under surcharge loading using

measured results from instrumented full-scale model tests. Bathurst et al. (2008) and Huang et al. (2010) conducted numerical simulations to investigate the effects of toe restraint conditions on the performance of GRS walls using the validated FLAC model. Results indicated that displacements at the bottom of the wall and reinforcement loads increased as the toe stiffness decreased. Huang et al. (2009) also investigated the effect of soil constitutive model on the behavior of GRS walls using FLAC. The investigated soil constitutive models included linearly elastic plastic Mohr-Coulomb model, modified Duncan-Chang hyperbolic model, and Lade's single hardening model. Simulated results for three constitutive models were evaluated by comparing with measured results at the end of construction and under surcharge loading conditions. Huang et al. (2009) concluded that the simple Mohr-Coulomb model is better suited for GRS walls that are at incipient failure conditions than for working stress conditions. Lade's model can simulate the shear dilatancy and strain softening behavior of soil during shearing; however, this model requires many parameters that lack physical meaning. On the other hand, the modified Duncan-Chang model can reasonably predict the response of GRS walls under work stress conditions, and the model parameters can be determined from conventional triaxial tests. Damians et al. (2014) investigate the effects of foundation compressibility and reinforcement stiffness on the behavior of reinforced soil walls using FLAC. Results indicated that facing displacements, connection loads, and reinforcement strains all increase, as foundation stiffness decreases, and the influence of reinforcement stiffness is greater than foundation stiffness for reinforced soil walls under working stress conditions. Yu et al. (2016) conducted a benchmark study to validate a numerical model using well-documented data for two instrumented GRS walls. This study described the detailed modeling procedures for GRS walls with high-quality data, including calibration of model parameters for backfill soil and geosynthetic reinforcement, and selection of constitutive models for backfill soil.

Guler et al. (2007) conducted a numerical investigation on the failure mechanisms of GRS walls using the strength reduction method. The finite element model in PLAXIS was first validated using data reported by Hatami and Bathurst (2005a, 2006) for three full-scale GRS walls, in which the backfill soil was simulated using hardening soil model and the geogrid was modeled using elastic element. A parametric study was carried out to investigate the effects of reinforcement length, reinforcement vertical spacing, and backfill soil type on the failure mechanism. Results indicated that sliding is the primary failure mode for GRS walls using both granular and cohesive backfill soil.

Mirmoradi and Ehrlich (2015, 2017) conducted a series of numerical studies to investigate the combined effects of toe condition, facing stiffness, backfill compaction, reinforcement stiffness, and wall height on the behavior of GRS walls under working stress conditions. The finite element model using PLAXIS was validated using data reported by Hatami and Bathurst (2005a, 2006) for a full-scale GRS wall. Results indicated that toe condition has an important effect on the reinforcement tensile force at the bottom section of the wall. For fixed toe conditions, as facing stiffness increase, horizontal toe load increases and reinforcement tensile forces decrease. For GRS

walls with greater reinforcement stiffness, the reinforcement forces are larger and the horizontal toe load is smaller. Also, the combined effects of different factors on the reinforcement tensile force distributions are limited to 4 m above the foundation level.

Numerical modeling studies have been conducted to investigate the static behavior of GRS bridge abutments. Skinner and Rowe (2005) conducted finite element analyses to investigate the behavior of GRS bridge abutments constructed on a yielding clay foundation. Zevgolis and Bourdeau (2007) studied the deformation behavior of GRS bridge abutments with different foundation soil conditions using the finite element program PLAXIS. Some numerical models have been validated using results from field monitoring and/or field loading tests, which provide more convincing insights on the behavior of GRS bridge abutments (Helwany et al. 2003, 2007; Wu et al. 2006a, b; Fakharian and Attar 2007; Ambauen et al. 2015).

Helwany et al. (2003) performed finite element analyses using the program DACSAR. The numerical model was validated using measurements for the Founders/Meadows GRS bridge abutment. The backfill soil was simulated as a nonlinear elastic material using the Duncan-Chang hyperbolic relationship, and the geosynthetic reinforcement was simulated as a linearly elastic material and was assumed to be perfectly bonded to backfill soils. Using the same abutment configuration, a parametric study was conducted to investigate the effects of foundation soil conditions on the behavior of GRS bridge abutments. Results showed that a loose sand foundation yielded much larger bridge footing settlements and lateral facing displacements than a dense sand foundation. Differential settlements between the bridge and approach embankment were acceptable for sand and medium-to-stiff clay foundation soils.

Wu et al. (2006a, b) conducted a series of finite element analyses to investigate the effects of bridge seat type, bridge seat width, backfill soil stiffness and strength, reinforcement spacing, and foundation stiffness on the load-bearing capacity of GRS bridge abutments. The allowable bearing pressures were determined based on a limiting displacement criterion or a limiting shear strain criterion. Results indicated that reinforcement spacing is the most important factor that influences the load-bearing capacity of a GRS bridge abutment. Based on the simulation results, design procedures were developed to determine the allowable bearing pressures considering footing type, reinforcement spacing, and soil conditions.

Helwany et al. (2007) performed finite element analysis of large-scale loading tests performed on the National Cooperative Highway Research Program (NCHRP) GRS bridge abutment (Wu et al. 2006a). The soil behavior was simulated using a cap plasticity model and the geosynthetic reinforcement was modeled using an elastic-plastic model. Simulated lateral facing displacements and bridge footing settlements were in close agreement with measurements. A corresponding parametric study indicated that soil friction angle, reinforcement spacing, and reinforcement stiffness are important factors that influence the behavior of GRS bridge abutments.

Fakharian and Attar (2007) also conducted an investigation of the Founders/Meadows bridge abutment using finite difference analysis. The backfill soil was modeled as Mohr-Coulomb with the Duncan-Chang hyperbolic relationship to account for nonlinear behavior. Simulated results were in generally satisfactory agreement with field measurements, including facing displacements, bridge footing settlements, earth pressures, and reinforcement strains.

Leshchinsky (2014) and Xie and Leshchinsky (2015) performed a series of parametric studies using limit analysis to investigate the optimal reinforcement design and failure mechanism of GRS bridge abutments. Results indicated that more closely spaced reinforcement in the upper part of a GRS wall can efficiently increase the ultimate bearing capacity, and also showed a curved failure surface between the heel of bridge footing and the toe of GRS bridge abutment for a footing setback distance of less than 1.35 m.

Ambauen et al. (2015) validated a finite element model using results from full-scale GRS walls under surcharge loading (Hatami and Bathurst 2006). A parametric study was conducted to investigate the effects of reinforcement type, reinforcement spacing, bridge footing location, bridge footing dimensions, and toe restraint conditions on the lateral earth pressure distributions, wall facing displacements, and reinforcement strains for service load conditions. Results indicate that close reinforcement vertical spacing resulted in increases of lateral earth pressures, but decreases of wall facing displacement, bridge footing settlements, and reinforcement strains.

## **2.2 Dynamic Response**

Segrestion and Bastick (1988) validated a dynamic finite element model in the program SUPERFLUSH with measured results from a shaking table test on a steel strip reinforced soil wall (Chida et al. 1982). Yogendrakumar et al. (1991) studied the seismic response of 6 m-high retaining walls reinforced with steel strips using the program TARA-3. Yogendrakumar and Bathurst (1992) and Bachus et al. (1993) conducted dynamic finite element modeling of reinforced soil walls subjected to blast loading using the programs RESBLAST and DYNA3D, respectively. Yogendrakumar et al. (1992) compared the dynamic response of reinforced soil walls under blast loading using both equivalent linear approach and nonlinear incremental approach, and found that the nonlinear incremental approach yielded better predictions when compared with measured results from a field test.

Cai and Bathurst (1995) conducted dynamic finite element modeling of GRS retaining walls with modular block facing using TARA-3. The cyclic shear behavior of backfill soil was modeled using a hyperbolic stress-strain relationship with Masing hysteretic rules for unloading and reloading. The reinforcement was modeled using a similar hysteretic model to capture the measured response of cyclic tensile tests on unconfined geogrid specimens. Slip elements were used to simulate the interactions between different components. The scaled El-Centro earthquake record with a PGA

of 0.25g was applied to the base of the model. Relative displacements and shear forces between blocks were greatest at the reinforcement elevations and shear capacity was exceeded at some locations. Cai and Bathurst (1995) concluded that the block-block interface properties are important for seismic design of GRS walls. Furthermore, predicted tensile forces in the reinforcement were smaller than calculated using the pseudo-static approach, which implied that the pseudo-static approach is conservative for the seismic design of GRS walls with modular block facing.

Bathurst and Hatami (1998, 1999) investigated the effect of different design parameters on the dynamic response of GRS walls with a rigid full-height facing panel using FLAC. The dynamic response of GRS walls was most sensitive to toe boundary condition (i.e., fixed toe vs. sliding toe). Both the facing displacements at the top and the relative displacement with respect to the toe were smaller for a wall with a sliding toe condition than with a fixed toe. Facing displacements decreased with increasing reinforcement stiffness and reinforcement length, but the effect was relatively small for a ratio of reinforcement length to wall height (L/H) greater than 0.7. Hatami and Bathurst (2000a) studied the effects of different structural design parameters on the fundamental frequency of GRS walls and concluded that fundamental frequency can be estimated with reasonable accuracy using a one-dimensional solution based on linear elastic theory. Results also showed that the fundamental frequency was not significantly affected by reinforcement stiffness, reinforcement length, toe restraint conditions and backfill soil friction angle, but was dependent on ground motion intensity and the width-to-height ratio (W/H) of the backfill. Hatami and Bathurst (2000b) simulated the dynamic response of GRS walls with modular block facing subjected to different ground motions. Facing displacements and reinforcement forces for GRS walls subjected to a single frequency harmonic motion were larger than the responses of walls subjected to actual earthquake ground motions with comparable predominant frequencies. The low-frequency ground motions with high intensity could result in significant structural responses for short-period GRS walls.

Helwany et al. (2001) validated a finite element model in the program DYNA3D using measured results from a small-scale shaking table test on a 0.9 m-high GRS wall with modular block facing. Nonlinear hysteretic behavior of the backfill soil under cyclic loading was simulated using the Ramberg-Osgood model with parameters determined from laboratory tests. The geotextile was modeled as a linearly elastic material. Helwany and McCallen (2001) investigated the influence of facing block connection on the static and dynamic behavior of GRS walls using the validated model. At the end of construction, the wall facing blocks with pin connections had smaller lateral facing displacements than without pin connections, while the facing blocks with pin connections experienced larger dynamic facing displacements. The smaller dynamic facing displacements for the wall without pin connections were due to smaller lateral earth pressures behind the wall facing, as the blocks without pin connections permitted more relative sliding between the blocks.

Ling et al. (2004) validated a finite element model for both static and dynamic analyses using a modified version of Diana-Swandyne II. A generalized plasticity model which accounted for the stress-dependent stiffness, strength and dilatancy, and cyclic hardening behavior, was used for the backfill soil. A bounding surface model was used to simulate the cyclic behavior of uniaxial geogrid. The interactions between different components were simulated using interface elements. The dynamic finite element model was validated using measured results from dynamic centrifuge tests. In these tests, the GRS walls were subjected to 20 cycles of sinusoidal excitation with a frequency of 2 Hz and acceleration amplitude of 0.2g. Simulated accelerations, facing displacements, crest settlement, and maximum tensile forces in the geogrid showed good agreement with measured results. Ling et al. (2005b) conducted a parametric study using the validated finite element model to investigate effects of soil and reinforcement properties, reinforcement length and spacing, and block interaction properties on the performance of GRS walls at the end of construction and under earthquake loading. Lateral facing displacements and crest settlement were mainly influenced by soil cyclic behavior, reinforcement layout, and earthquake motions. The effects of reinforcement vertical spacing on facing displacements, reinforcement forces, and lateral earth pressures were more significant than the reinforcement length.

El-Emam et al. (2004) and Fakharian and Attar (2007) validated FLAC models using measured results from reduced-scale shaking table tests on GRS walls with a rigid full-height facing panel conducted at RMC (El-Emam and Bathurst 2004, 2005, 2007). Above numerical model validations have been based on either reduced-scale shaking table tests or dynamic centrifuge tests, both of which have disadvantages such as model size effects, stress level effects, and boundary condition effects. The large-scale shaking table tests on 2.8 m-high GRS walls with modular block facing conducted by Ling et al. (2005a) have provided valuable data for validation of dynamic numerical models (Ling et al. 2010; Lee et al. 2010; Guler et al. 2012; Ren et al. 2016). Ling et al. (2010) validated a dynamic finite element model using experimental results and improved the soil and geosynthetic models (Ling 2003; Ling et al. 2005b). The unified general plasticity model for soil was improved by considering the effect of soil density, and the S-shaped load-strain relationship was accounted for to simulate the cyclic behavior of geogrid. Lee et al. (2010) also simulated the large-scale shaking table tests using the finite element program LS-DYNA. The backfill soil was simulated using a geological cap model and the geogrid reinforcement was simulated using a plastic-kinematic model with a bilinear stress-strain curve. Lee and Chang (2012) conducted a parametric study using the validated program to investigate the effects of different design parameters, including wall height, wall batter angle, backfill soil friction angle, reinforcement spacing, and reinforcement stiffness, on the seismic performance of GRS walls. Results showed that GRS walls become less stable with a decreasing batter angle (e.g., more near vertical) for the wall facing and a close reinforcement vertical spacing of 0.2 m is effective on reducing wall deformations and reinforcement forces. Maximum tension line is close to the wall facing, which indicates that connection strength is important for the seismic design for internal stability.

Helwany et al. (2012) validated a 3-D ABAQUS finite element model using measured results from the full-scale shaking table tests on the GRS bridge abutment. The backfill soil was simulated using a cyclic model with isotropic/kinematic hardening and the geotextile was modeled using membrane elements. Interface elements that allow sliding and separation were also placed between blocks and reinforcement, between soil and reinforcement, and between blocks and soil. Parametric studies were conducted to investigate the influences of various design parameters, including backfill soil friction angle, reinforcement stiffness, reinforcement spacing, bridge height, bridge span, and earthquake ground motion, on the seismic performance of GRS bridge abutments. Simulation results indicated that GRS bridge abutments would generally experience small seat settlements (less than 5 cm) but relatively large facing lateral displacements (up to 20 cm) for strong earthquake motions.

### **2.3 Summary**

Overall, the field investigations of Yen et al. (2011) indicated good seismic performance of GRS bridge abutments in terms of facing displacements and bridge seat settlements. The shaking table tests by Helwany et al. (2012) indicated that GRS bridge abutments have satisfactory performance when subjected to longitudinal shaking. However, more experiments evaluations and numerical simulations are needed to understand the potential issues and performance characteristics for various configurations under dynamic loading. To address these needs, this report presents a numerical investigation on the dynamic response of MSE bridge abutments for shaking in the longitudinal direction.

## Chapter 3 Numerical Simulation of Shaking Table Tests on MSE Bridge Abutments

### 3.1 Introduction

The two-dimensional finite difference program *FLAC* 7.0 (Itasca Consulting Group 2011) was used for the current investigation to simulate the shaking table tests on half-scale MSE bridge abutments. The shaking table test program performed as part of this project is presented in Table 3.1, and the details are reported by McCartney et al. (2018). This report focuses on shaking table tests on MSE bridge abutments using geosynthetics and subjected to shaking in the longitudinal direction (Tests 1-4).

Table 3.1 Shaking table test program

Test	Variable	Bridge surcharge stress (kPa)	Reinforcement spacing (m)	Reinforcement stiffness (kN/m)	Global stiffness (kN/m) <sup>1</sup>	Shaking direction
1	Baseline case	66	0.15	380	2352	Longitudinal
2	Bridge surcharge stress	43	0.15	380	2352	Longitudinal
3	Reinforcement spacing	66	0.30	380	1267	Longitudinal
4	Reinforcement stiffness	66	0.15	190	1176	Longitudinal
5	Steel reinforcement	66	0.15	4800	29709	Longitudinal
6	Shaking direction	66	0.15	380	2352	Transverse

<sup>1</sup> defined as  $\sum_{i=1}^n J_i / h$ , where  $J_i$  = index stiffness of each reinforcement layer,  $n$  = number of reinforcement layers, and  $h$  = lower wall height (Bathurst et al. 2009).

### 3.2 Model Geometry

The model geometry for the baseline MSE bridge abutment (Test 1) in the longitudinal direction is shown in Figure 3.1. The bridge beam is placed on a bridge seat that rests on the MSE bridge abutment at one end and on a concrete support wall at the other end. The back of the abutment is supported by a reaction wall. The bridge beam has dimensions of 6.4 m  $\times$  0.45 m (length  $\times$  height) and a contact length of 0.45 m on the bridge seat. The seismic joint between the bridge seat and bridge beam is 25 mm. The bridge seat has a height of 0.6 m and length of 0.65 m for the bottom surface, and a setback distance of 0.15 m from the back of wall facing. The clear distance between the top of the wall facing and bottom of the bridge beam is 0.15 m. The MSE bridge abutment has a total height of 2.7 m, consisting of a 2.1 m-high lower MSE wall and a 0.6 m-high upper wall, resting on a 0.15 m-thick foundation soil layer. The lower MSE wall was constructed in fourteen 0.15 m-thick soil lifts. Each lift includes one facing block, one lift of soil, and reinforcement layers in the longitudinal direction and the transverse direction. The longitudinal reinforcement layers extend 1.63 m from the wall facing, and the transverse reinforcement layers extend 2.1 m to the reaction wall. The transverse reinforcement layers are offset by 25 mm vertically from the longitudinal reinforcement layers. The upper wall consists of four 0.15 m-thick soil lifts with reinforcement layers only in the transverse direction.

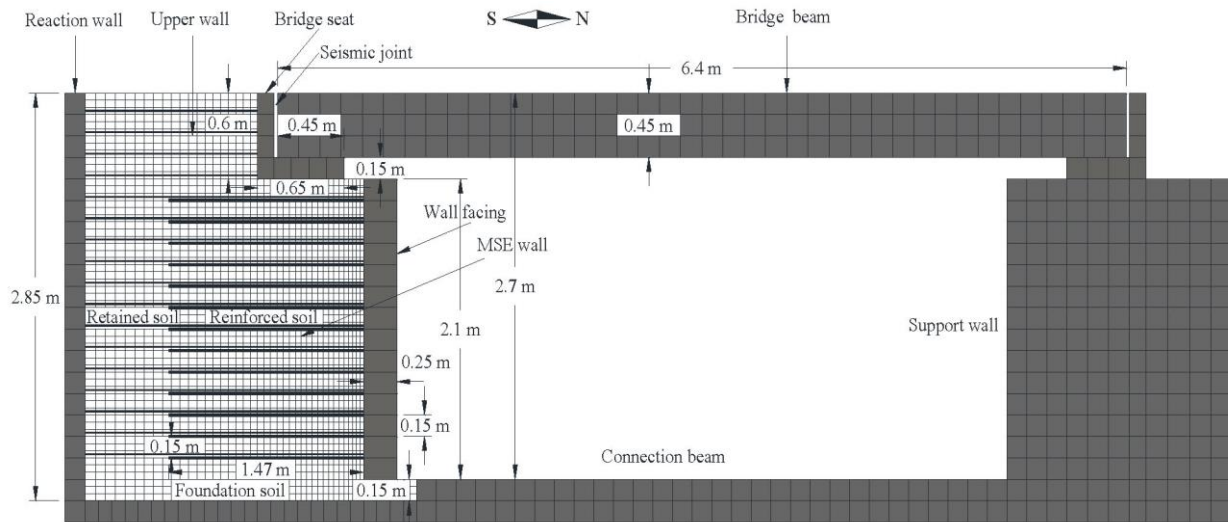


Figure 3.1 Model geometry (Test 1) for the baseline shaking table test with shaking in the longitudinal direction.

### 3.3 Material Model and Properties

#### 3.3.1 Soils

The soil has a coefficient of uniformity  $C_u = 6.1$ , coefficient of curvature  $C_z = 1.0$ , mean particle size  $D_{50} = 0.85$  mm, and is classified as a well-graded sand (SW) according to the USCS (Unified Soil Classification System). The specific gravity  $G_s = 2.61$ , the fines content (i.e., passing No. 200 sieve) = 2.5%, and the maximum and minimum void ratios are  $e_{max} = 0.853$  and  $e_{min} = 0.371$ , respectively. The soil properties are summarized in Table 3.2.

Table 3.2 Soil properties.

Property	Value
Specific gravity, $G_s$	2.61
Coefficient of uniformity, $C_u$	6.1
Coefficient of curvature, $C_z$	1.0
Mean particle size, $D_{50}$ (mm)	0.85
Relative density, $D_r$ (%)	70
Dry density, $\rho_d$ (kg/m <sup>3</sup> )	1808
Initial void ratio, $e_0$	0.515
Maximum void ratio, $e_{max}$	0.853
Minimum void ratio, $e_{min}$	0.371
Peak friction angle, $\phi'_p$ (°)	51.3
Dilation angle, $\psi$ (°)	13.0

For static analysis, the backfill soil was modeled as a nonlinear elastic-plastic material with a stress-strain curve represented by a Duncan-Chang hyperbolic curve (Duncan et al. 1980) and a Mohr-Coulomb failure criterion. This model can capture the nonlinear stress-strain behavior before the peak shear strength and dilation behavior. Details of the soil model are reported by Zheng and Fox (2016, 2017).

For dynamic analysis, a robust, relatively simple, total stress model referred to as UBCHYST was used in this study. UBCHYST was developed by Byrne and Naesgaard (2010) and was implemented as a User-Defined Model (UDM) in *FLAC* by Mikola and Sitar (2015). The UBCHYST model is intended to be used with “undrained” strength parameters in low permeability clayey and silty soils, in highly permeable granular soils, where excess pore water would dissipate as generated, or in non-saturated granular soils where negligible effects of pore water are expected (as in this study). The model can capture the reduction in secant modulus with strain.

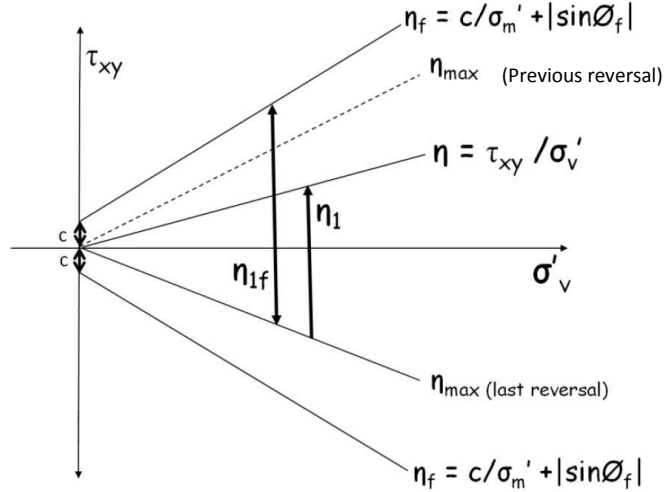


Figure 3.2 UBCHYST model key variables (Byrne and Naesgaard 2010).

In the hysteretic model, the tangent shear modulus  $G_t$  is a function of the peak shear modulus times a reduction factor that is a function of the developed stress ratio and change in stress ratio to reach failure. This function is illustrated in Figure 3.2 and  $G_t$  is expressed as follows:

$$G_t = G_{\max} \times \left(1 - \left(\frac{\eta_1}{\eta_{1f}}\right)^{n_1} \times R_f\right)^n \times \text{mod1} \times \text{mod2} \times \text{mod3} \quad (3.1)$$

where

$G_{\max}$  = small strain shear modulus

$\eta$  = developed stress ratio ( $\tau_{xy} / \sigma'_v$ )

$\eta_1$  = change in stress ratio  $\eta$  ( $\tau_{xy} / \sigma'_v$ ) since last reversal ( $\eta_f - \eta_{\max}$ )

$\eta_{\max}$  = maximum stress ratio ( $\eta$ ) at last reversal

$\eta_{1f}$  = change in stress ratio to reach failure envelope in direction of loading ( $\eta_f - \eta_{\max}$ )

$\eta_f$  =  $(\sin \phi'_f + c' \cos \phi'_f / \sigma'_v)$

$\phi'_f$  = peak friction angle

$c'$  = cohesion

$\tau_{xy}$  = developed shear stress in horizontal plane

$\sigma'_v$  = vertical effective stress

$n_1, n, R_f$  = calibration parameters

*mod1* = reduction factor for first-time or virgin loading

*mod2* = optional function for permanent modulus reduction with large strain

*mod3* = optional function for cyclic degradation of modulus with strain or number of cycles

In this study, the small strain shear modulus  $G_{max}$  is estimated using the empirical relationship proposed by Menq (2003), as follows:

$$G_{max} = C_{G3} \times C_u^{b1} \times e^x \times \left( \frac{\sigma'_m}{p_a} \right)^{n_G} \quad (3.2)$$

where  $C_{G3} = 67.1$  MPa,  $b1 = -0.2$ ,  $x = -1 - \left( \frac{D_{50}}{20} \right)^{0.75}$ , and  $n_G = 0.48 \times C_u^{0.09}$ .

The model parameters were calibrated by comparing cyclic simple shear response to the modulus reduction curves and damping curves calculated using empirical relationships from published literature (Darendeli 2001; Menq 2003). The shear modulus reduction curve proposed by Darendeli (2001) is expressed as follows:

$$\frac{G}{G_{max}} = \frac{1}{1 + \left( \frac{\gamma}{\gamma_r} \right)^a} \quad (3.3)$$

where  $\gamma_r$  is the reference strain (%) (at  $G/G_{max} = 0.5$ ),  $a$  is the curvature coefficient, and the values are calculated as follows (Menq 2003):

$$\gamma_r = 0.12 \times C_u^{-0.6} \times \left( \frac{\sigma'_m}{p_a} \right)^{0.5 \times C_u^{-0.15}} \quad (3.4)$$

$$a = 0.86 + 0.1 \times \log \left( \frac{\sigma'_m}{p_a} \right) \quad (3.5)$$

Alternatively, Darendeli (2001) noted that  $a$  could be defined as a constant equal to  $a = 0.92$ . The damping curve proposed by Darendeli (2001) is expressed as

$$D_s = D_{nonlinear} + D_{s,min} \quad (3.6)$$

where  $D_{s,min}$  is the small strain damping ratio calculated as

$$D_{s,min} = 0.55 \times C_u^{0.1} \times D_{50}^{-0.3} \times \left( \frac{\sigma'_m}{p_a} \right)^{-0.08} \quad (3.7)$$

and  $D_{nonlinear}$  is the damping for Masing behavior calculated as

$$D_{nonlinear} = b \times \left( \frac{G}{G_{max}} \right)^p \times D_{Masing} \quad (3.8)$$

where  $b = 0.6329 - 0.0057 \times \ln(N)$ ,  $N$  = number of cycles (Menq 2003),  $p = 0.1$  (Darendeli 2001), and the value of  $D_{Masing}$  is estimated using the following equation:

$$D_{Masing} = c_1 \times D_{Masing,a=1.0} + c_2 \times D_{Masing,a=1.0}^2 + c_3 \times D_{Masing,a=1.0}^3 \quad (3.9)$$

where:

$$D_{Masing,a=1.0}(\%) = \frac{100}{\pi} \left[ 4 \frac{\gamma - \gamma_r \ln \left( \frac{\gamma + \gamma_r}{\gamma_r} \right)}{\frac{\gamma^2}{\gamma + \gamma_r}} - 2 \right] \quad (3.10)$$

$$c_1 = -1.1143a^2 + 1.8618a + 0.2523$$

$$c_2 = 0.0805a^2 - 0.0710a - 0.0095$$

$$c_3 = -0.0005a^2 + 0.0002a + 0.0003$$

The calibrated modulus reduction curves and damping curves using the hysteretic soil model, and corresponding calculated curves using the empirical relationships (Darendeli 2001; Menq 2003) are shown in Figure 3.3. Results indicate that the simulated and calculated modulus reduction curves are in good agreement, while the simulations overestimate the damping ratios for shear strain greater than 0.1% strain. The calibrated model parameters are summarized in Table 3.3.

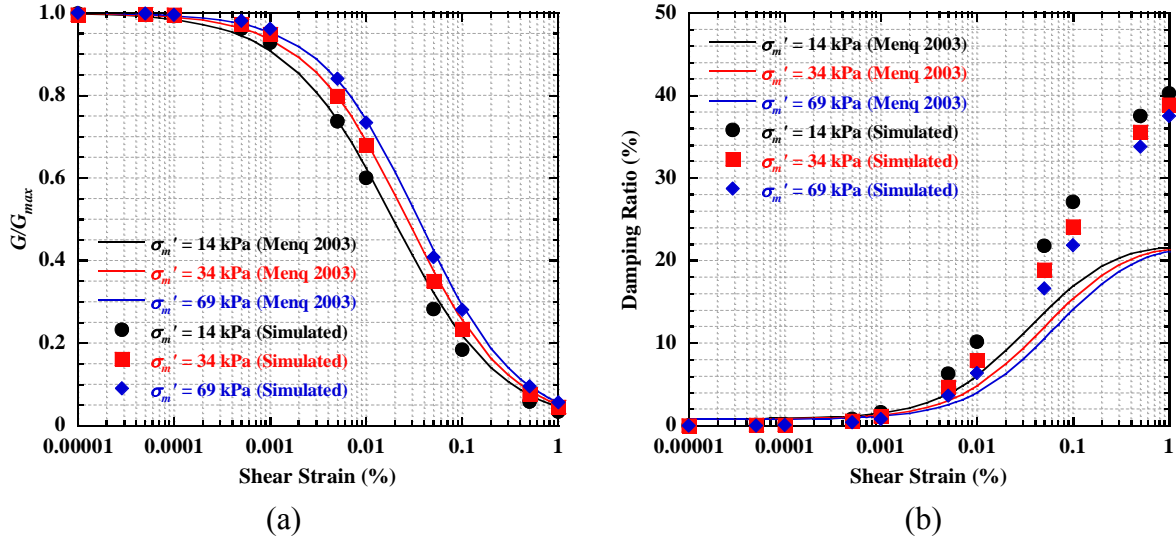


Figure 3.3 Comparison of simulated (FLAC) and calculated (Darendeli 2001; Menq 2003) results: (a) modulus reduction curves; (b) damping curves.

Table 3.3 UBCHYST model parameters.

Parameter	Value
Friction angle, $\phi'$ ( $^\circ$ )	51.3
Cohesion, $c'$ (kPa)	0
Tensile strength, $t$ (kPa)	0
Dilation angle, $\psi$ ( $^\circ$ )	0
Small strain shear modulus, $G_{max}$ (MPa)	Stress-dependent
Bulk modulus, $B$ (MPa)	$= G_{max}$
Atmospheric pressure, $p_a$ (kPa)	101.3
Hysteretic parameter, $H_n$	6.0
Hysteretic parameter, $H_{n1}$	1.0
Hysteretic parameter, $H_{rf}$	0.98
Hysteretic parameter, $H_{rm}$	1.0
Hysteretic parameter, $H_{dfac}$	0

The shear stress-strain relationships from the numerical simulations for different mean effective stresses and cyclic shear strain amplitudes are shown in Figure 3.4. The model exhibits hysteretic soil behavior that is consistent with that observed for sands. However, the model cannot capture the compression during dynamic loading that is typically observed in sands, as shown in Figure 3.5. In sands, volumetric contraction is expected to occur during each cycle of dynamic loading. However, the results in Figure 3.5 indicate that using a positive dilation angle leads to volumetric expansion of the sand, which is not realistic. Accordingly, a zero dilation angle is used in the analyses so that the sand will show some contraction during cyclic loading. However, this choice

is still not ideal as all of the contraction occurs on the first cycle and additional contraction is not observed during repeated cycling. This is an issue that can be improved in future constitutive modeling studies.

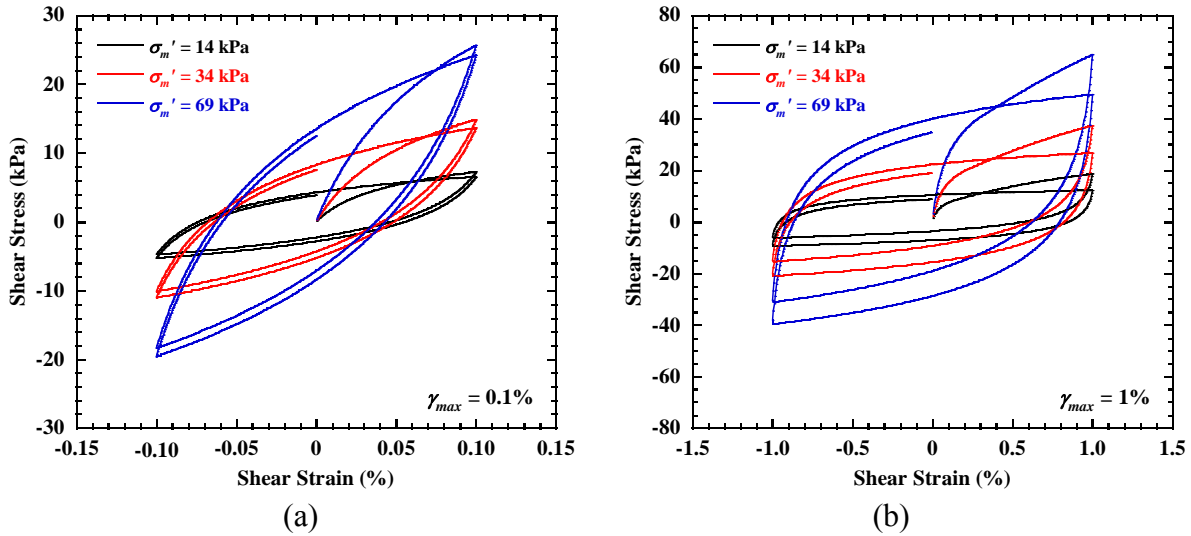


Figure 3.4 Simulated shear stress vs. shear strain: (a)  $\gamma_{max} = 0.1\%$ ; (b)  $\gamma_{max} = 1\%$ .

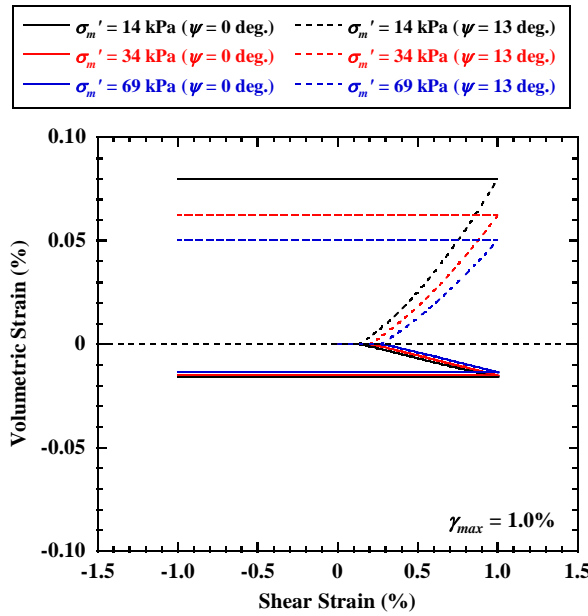


Figure 3.5 Simulated volumetric strain vs. shear strain at  $\gamma_{max} = 1\%$ .

### 3.3.2 Reinforcements

The geosynthetic reinforcement is a uniaxial high-density polyethylene (HDPE) geogrid (LH800) manufactured by Tensar International Corp. According to tensile tests on single rib specimens at a strain rate of 10%/min (ASTM D6637), the geogrid has secant stiffness at 5% strain  $J_{5\%} = 380$  kN/m and ultimate strength  $T_{ult} = 38$  kN/m in the machine direction, and  $J_{5\%} = 80$  kN/m and  $T_{ult} = 4$  kN/m in the cross-machine direction. For Tests 1, 2, and 4, reinforcement layer was placed with each soil lift to give a vertical spacing  $S_v = 0.15$  m. For Test 3, reinforcement layers were placed with every other soil lift to give  $S_v = 0.3$  m. For Test 4, every other rib of the geogrid in the transverse direction was cut to give a reduced secant stiffness of  $J_{5\%} = 190$  kN/m.

The geogrid reinforcement layers were simulated using linearly elastic cable elements. Both the longitudinal and transverse reinforcement layers were included in each lift and have a vertical offset of 25 mm. The longitudinal reinforcement layers with a tensile stiffness of 380 kN/m (machine direction) and length of 1.47 m were rigidly connected to the facing blocks. The transverse reinforcement layers with a tensile stiffness of 80 kN/m (cross-machine direction) and length of 2.1 m were not connected with the facing blocks.

### 3.3.3 Structural Components

The concrete facing blocks, bridge seat, reaction wall, connection beam, and support wall were modeled as elastic materials with unit weight  $\gamma = 23.5$  kN/m<sup>3</sup>, elastic modulus  $E = 20$  GPa, and Poisson's ratio  $\nu = 0.2$ . A longitudinal slice of the bridge beam with unit width was modeled as a solid block composed of elastic elements having an equivalent unit weight  $\gamma_{eq} = 37.8$  kN/m<sup>3</sup> to produce an average vertical stress of 66 kPa on the lower MSE wall for Tests 1, 3, and 4. For Test 2 (reduced bridge surcharge stress), an equivalent unit weight  $\gamma_{eq} = 25.1$  kN/m<sup>3</sup> for the bridge beam was used to produce an average vertical stress of 43 kPa.

### 3.3.4 Interfaces

Various interfaces between soil, geogrid, block, and structures were simulated using interface elements with Coulomb sliding behavior. The bearing pads between the bridge beam and seat, and support wall were simulated using interface elements with a friction coefficient of 0.4 (Caltrans 2004). The properties for different interfaces are presented in Table 3.3.

Table 3.4 Interface properties.

Property	Soil-geogrid	Soil-block/ bridge seat	Block-block	Bridge-bridge seat (bearing pad)
Friction angle	46.7 °	39.1 °	36.0 °	21.8 °
Adhesion	3.4 kN/m	1.3 kPa	58 kPa	0

### 3.4 Static Modeling Procedures

For the static analysis, the MSE bridge abutment model was constructed in stages. The lower MSE abutment was first constructed in layers on top of the foundation soil, with each layer consisting of one soil lift, one facing block, and the necessary interfaces. Geogrid reinforcement layers were placed at specified elevations, depending on the simulation. A temporary uniform surcharge stress of 8 kPa was applied to the top surface of each soil lift to simulate the effect of compaction and then removed prior to application of the next lift. Once the lower MSE wall was completed, the bridge seat was placed on top of the abutment, the upper wall was similarly constructed in layers behind the bridge seat. The bridge beam then was placed on the bridge seat and support wall with the specified unit weight. For each construction stage, the numerical model was resolved to equilibrium under gravitational forces.

### 3.5 Dynamic Modeling Procedures

For the dynamic analysis, the first earthquake motion from the shaking table tests (i.e., the 1940 Imperial Valley motion, El Centro Station), was simulated for comparison with the shaking table test results. This was done to avoid the complication of considering the effects of backfill densification and cyclic softening that may occur when applying several earthquake motions in sequence during shaking table testing. For each test that was simulated, the measured actual acceleration time history for the shaking table during the Imperial Valley motion was applied at the bottom boundary of the model. An example of the acceleration time history for Test 1 during the Imperial Valley motion is shown in Figure 3.6 and indicates a peak horizontal acceleration (PHA) of  $0.42g$ . For each case, 0.8% Rayleigh damping was assumed for the soil, according to the small strain damping ratio  $D_{s,min}$  in Figure 3.3.

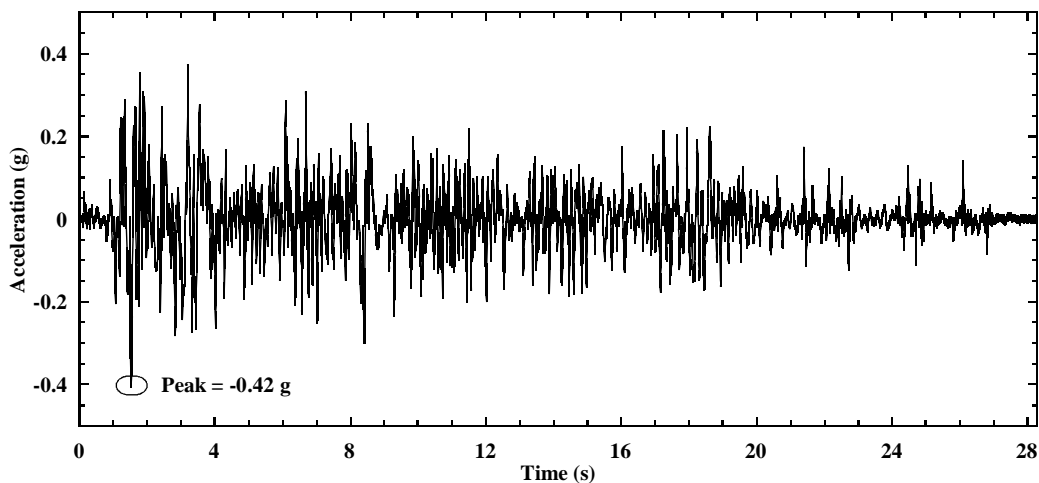


Figure 3.6 Acceleration time history for shaking table during the 1940 Imperial Valley earthquake motion in Test 1.

### **3.6 Simulation Results**

This section presents comparison of simulated and measured results for the longitudinal shaking tests on the MSE bridge abutments (Tests 1-4), including facing displacements, bridge seat and bridge beam displacements, accelerations, vertical and lateral stresses, and reinforcement strains. Instrumentation details for the shaking table tests are reported by McCartney et al. (2018). Horizontal displacements and accelerations toward the north, outward displacements for the front wall and downward displacements (i.e., settlements) for the bridge seat are defined as positive (see orientation in Figure 3.1).

#### ***3.6.1 Facing Displacements***

Time history plots of incremental facing displacements for Test 1 during the Imperial Valley motion are shown in Figure 3.7, with all values taken relative to initial facing displacements before the start of shaking. The maximum (i.e., during shaking) and residual (i.e., after shaking) facing displacements at the top generally are larger than at the bottom for both simulated and measured results. The simulated facing displacements indicate relatively flat response after reaching the peak values, while the measured results show stronger variations during shaking.

Profiles of the incremental maximum dynamic facing displacement during the Imperial Valley motion are shown in Figure 3.8(a). The simulated profiles for all four tests display similar shapes with incremental facing displacements generally increasing with elevation and highest values measured near or at the top of the wall. The magnitudes of simulated and measured maximum dynamic facing displacement are in reasonable agreement. The profiles of the incremental residual facing displacement are shown in Figure 3.8(b). The simulated residual facing displacements are larger than the measured values, especially toward the top of the wall, but show similar trends. Tests 3 and 4 have the largest facing displacement, which indicates that the reinforcement vertical spacing and reinforcement stiffness are important variables with regard to facing displacements under dynamic loading. The residual facing displacements for Test 2 are larger than for Test 1, which agrees with the measured data, due to smaller backfill soil modulus associated with reduced surcharge stress.

The highest values of incremental maximum dynamic and residual facing displacement for each test are presented in Figure 3.9. The simulated highest dynamic facing displacements are in good agreement with the measured displacements, while the simulated highest residual facing displacements are approximately 2 to 4 times larger than the measured values. In general, the numerical model accurately captures the effects of reinforcement spacing, reinforcement stiffness, and bridge surcharge stress on facing displacements under dynamic loading, but overestimates the magnitudes of residual facing displacement.

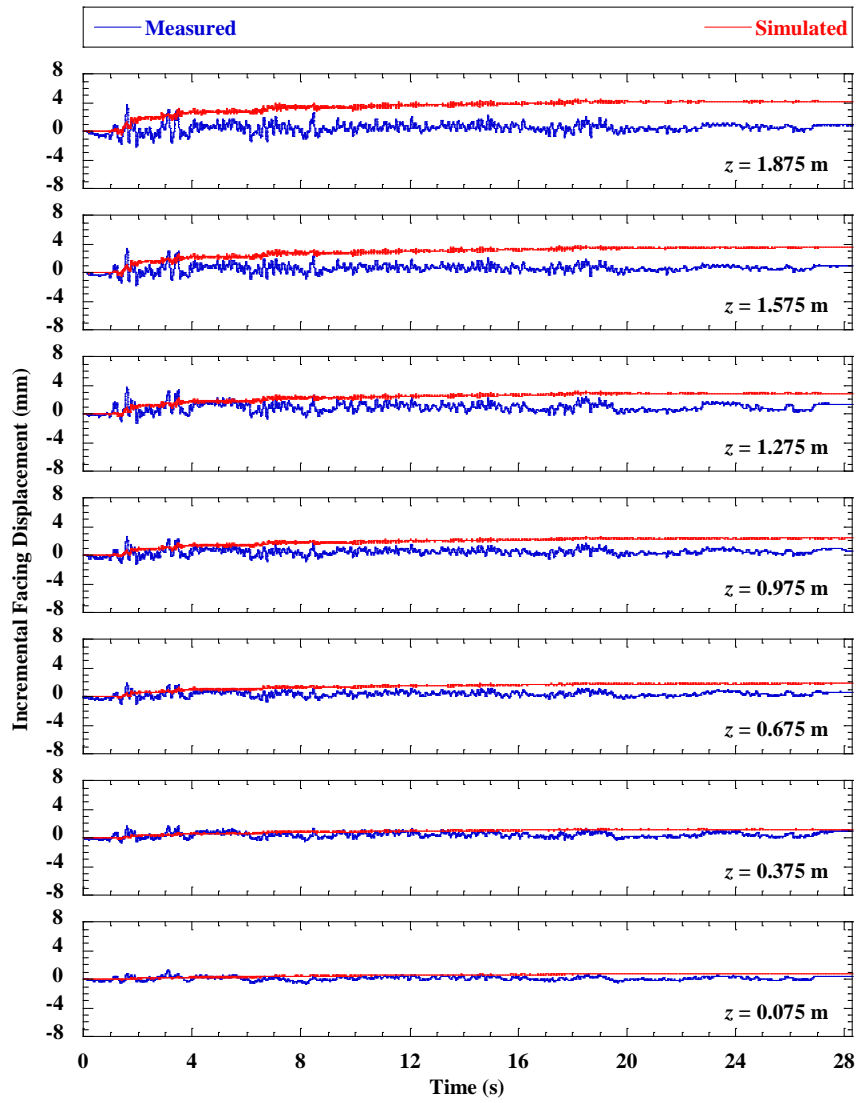


Figure 3.7 Time histories of incremental facing displacement during the Imperial Valley earthquake motion in Test 1.

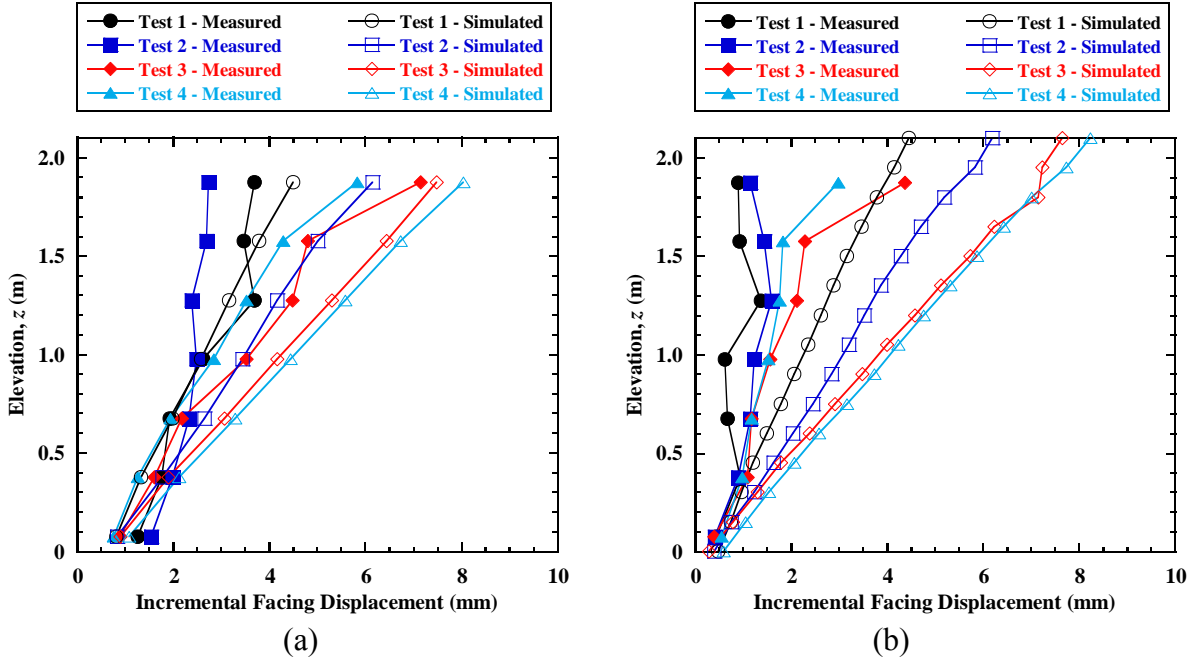


Figure 3.8 Profiles of incremental facing displacement for the Imperial Valley motion: (a) maximum dynamic; (b) residual.

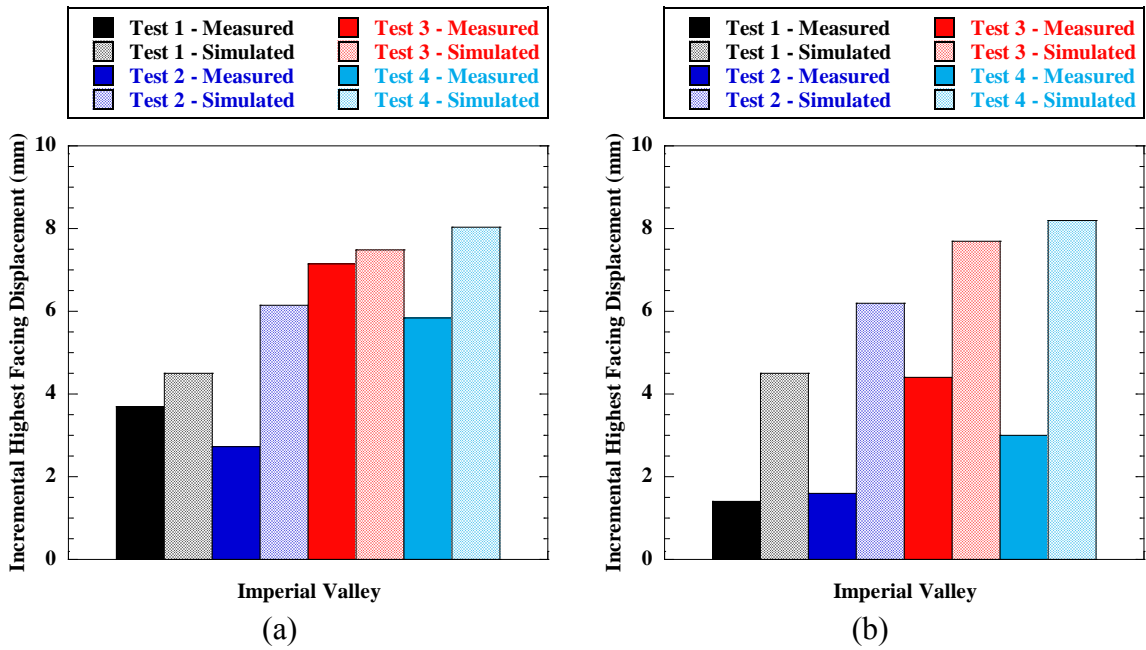


Figure 3.9 Incremental highest facing displacements for the Imperial Valley motion: (a) maximum dynamic; (b) residual.

### 3.6.2 Bridge Seat and Bridge Beam Displacements

Time history of the average bridge seat settlement for Test 1, taken as the average settlement of the toe and heel of the bridge seat, is shown in Figure 3.10. The simulated bridge seat settlement increased significantly to approximately 1.0 mm at  $t = 2$  s, and increased slightly thereafter with a relatively flat response. The measured average settlement, taken as the average of the four top corners of the bridge seat, had the maximum value of 3.0 mm at  $t = 3$  s, but most of the dynamic settlement were recovered after shaking. The simulated residual bridge seat settlement of 1.6 mm is in good agreement with the measured residual value of 1.4 mm. The simulated residual average bridge seat settlement for each test are compared with the measured values in Figure 3.11, and indicate good agreement.

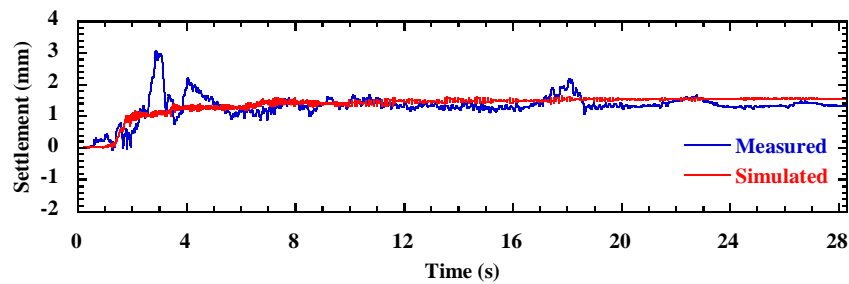


Figure 3.10 Time history of incremental average bridge seat settlement for Test 1 during the Imperial Valley motion.

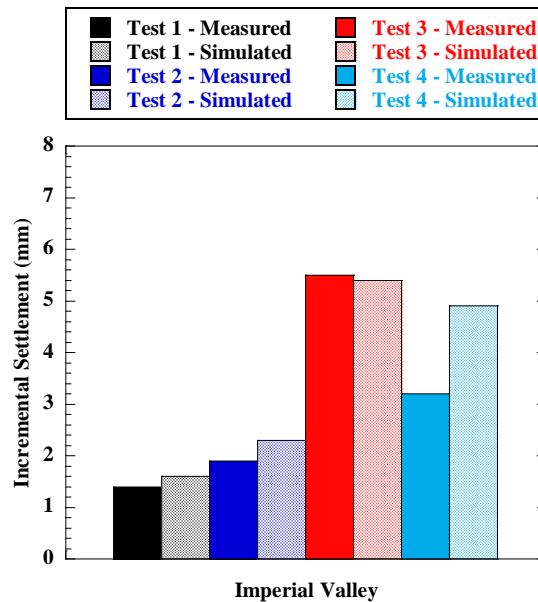


Figure 3.11 Incremental residual bridge seat settlement for Test 1 during the Imperial Valley motion.

During shaking, the bridge beam interacts with the MSE abutment and support wall through friction developed between the bearing pads and concrete, and the bridge beam may potentially contact the back wall of the bridge seat. As the bridge beam moved relative to the bridge seat, the width of seismic joint also changed, as shown in Figure 3.12. In general, the simulated results show a more flat response than measured data. The simulated residual width was 21.9 mm, which is smaller than the measured value of 27.2 mm. Joint closure did not occur in both the experiment and simulation for the Imperial Valley motion, and thus no impact force between the bridge beam and bridge seat.

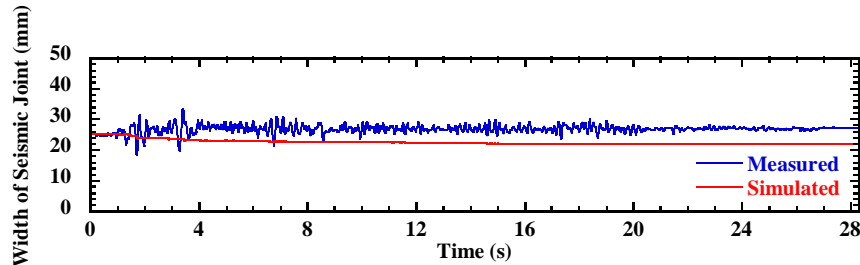


Figure 3.12 Time history of seismic joint width for Test 1 during the Imperial Valley motion.

### 3.6.3 Accelerations

Time histories of horizontal acceleration for the wall facing, reinforced soil zone, and retained soil zone, in Test 1 are shown in Figure 3.13, Figure 3.14, and Figure 3.15, respectively. Similar to facing displacements, horizontal accelerations increase with elevation and thus indicate increasing amplification toward the top of the MSE bridge abutment. The amplitudes of simulated acceleration generally are larger than the measured values for all three sections, especially near the top of the wall.

Time histories of horizontal acceleration for the bridge seat and bridge beam are shown in Figure 3.16. The simulated accelerations for the bridge seat and bridge beam generally match the trends with the measured accelerations but with larger amplitudes. The simulated peak acceleration of 0.79g for the bridge seat is larger than the measured peak value of 0.63g.

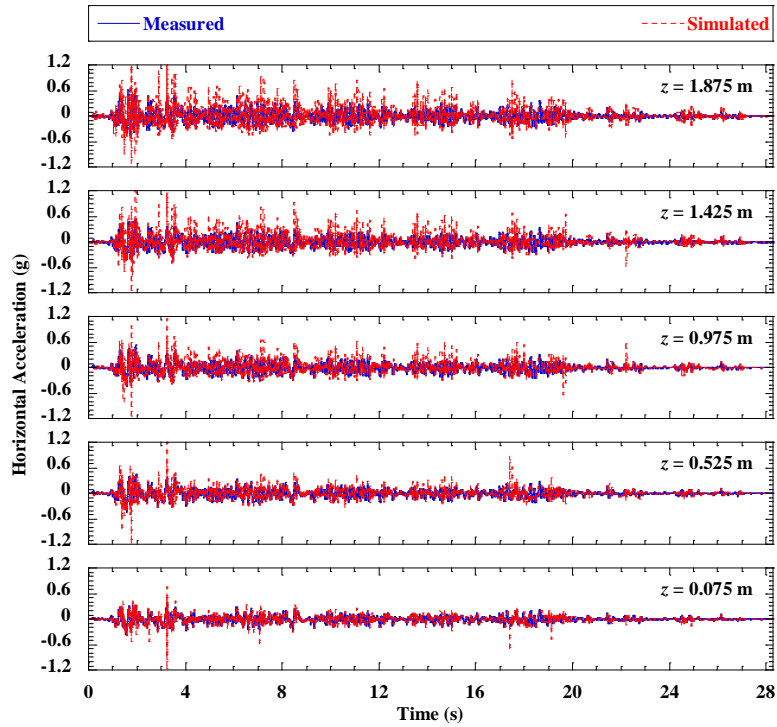


Figure 3.13 Time histories of horizontal acceleration for wall facing in Test 1 during the Imperial Valley motion.

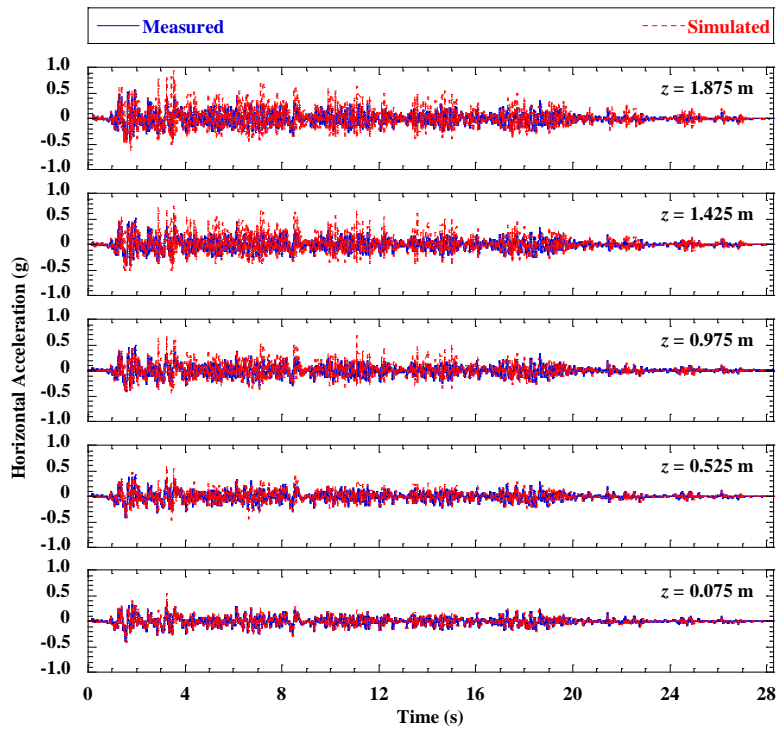


Figure 3.14 Time histories of horizontal acceleration for reinforced soil zone in Test 1 during the Imperial Valley motion.

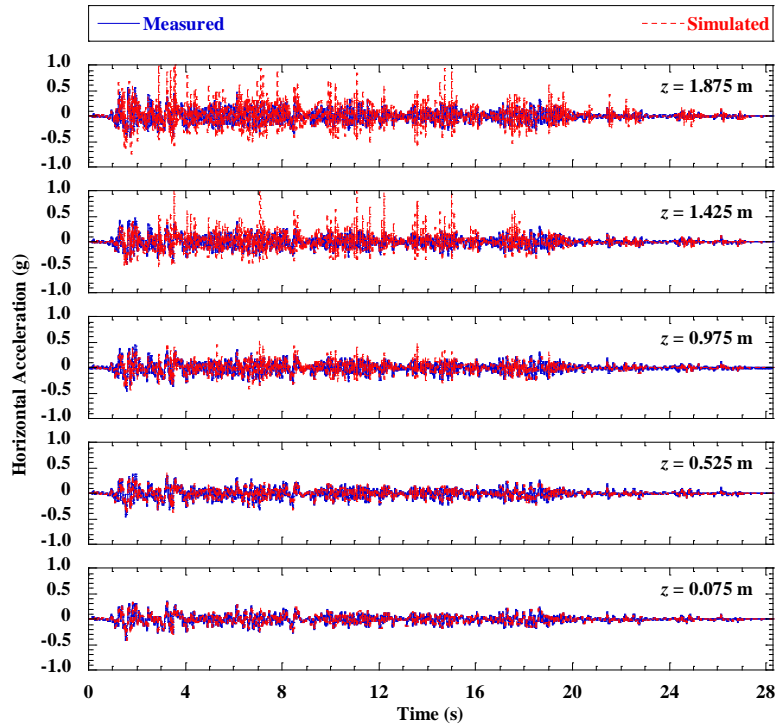
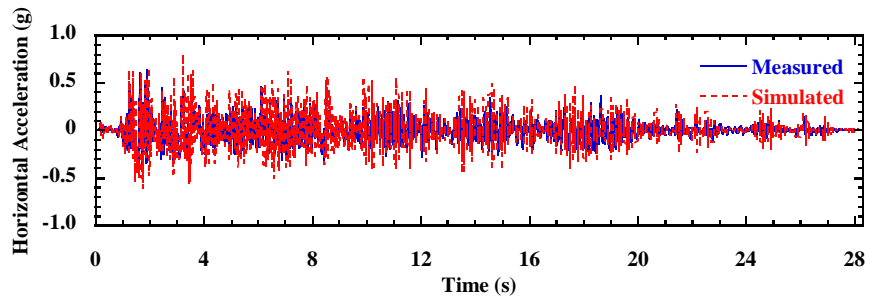
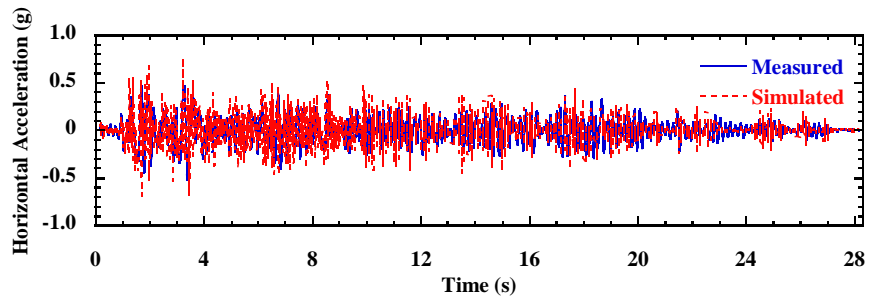


Figure 3.15 Time histories of horizontal acceleration for retained soil zone in Test 1 during the Imperial Valley motion.



(a)



(b)

Figure 3.16 Time histories of horizontal acceleration in Test 1 during the Imperial Valley motion: (a) bridge seat; (b) bridge beam.

### 3.6.4 Vertical and Lateral Stresses

Time histories of soil vertical stress and lateral stress behind the wall facing in Test 1 are shown in Figure 3.17 and Figure 3.18. The simulated dynamic vertical and lateral stresses are in reasonable agreement with the measured stresses except at the bottom and top of the wall.

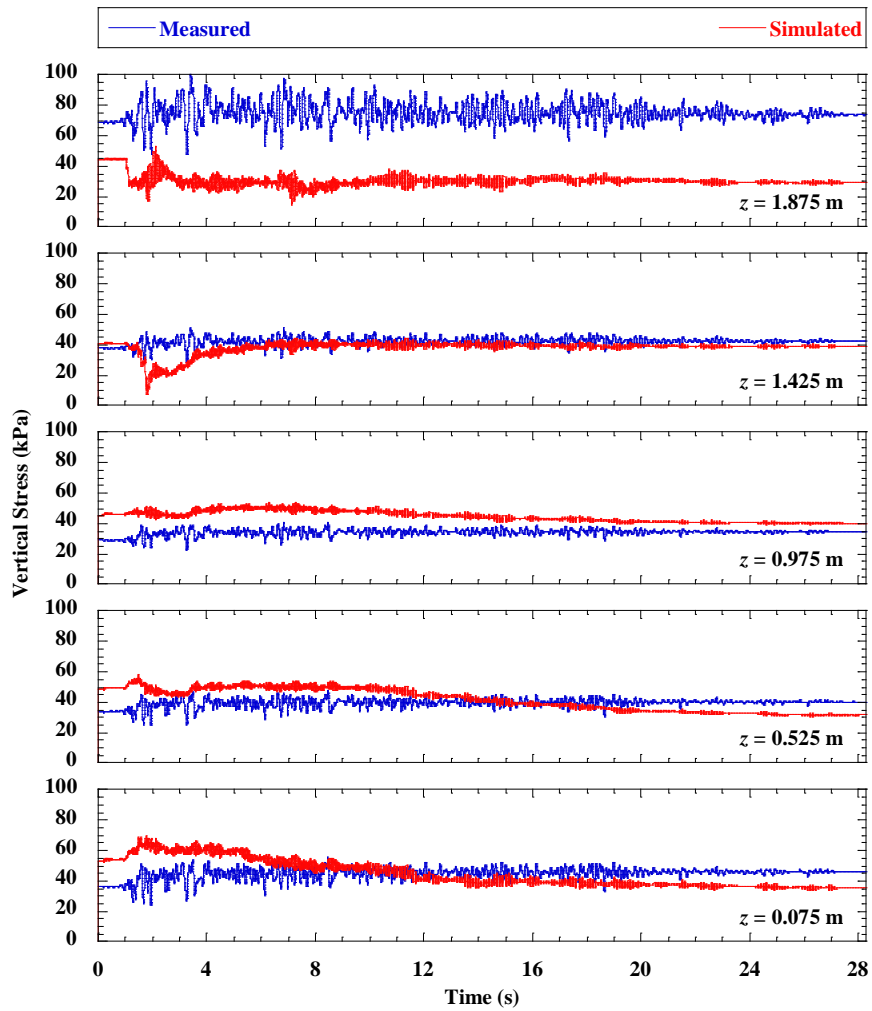


Figure 3.17 Time histories of vertical soil stress for Test 1 during the Imperial Valley motion.

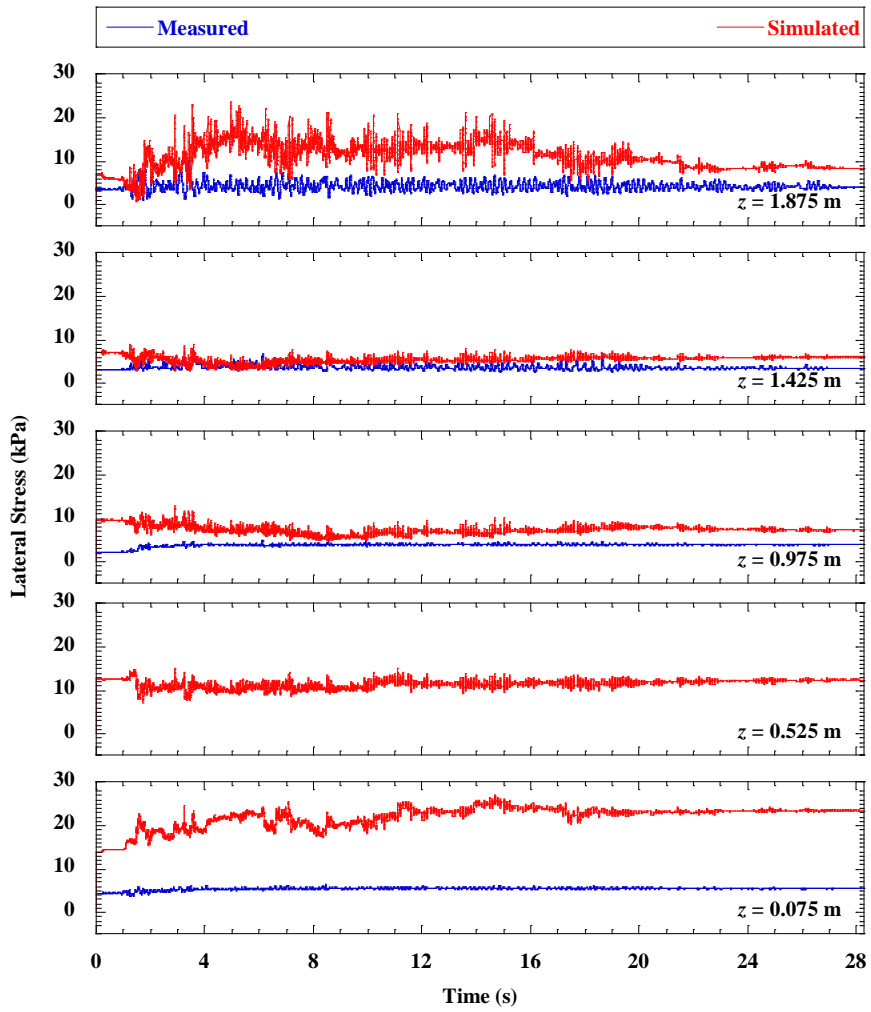


Figure 3.18 Time histories of lateral soil stress for Test 1 during the Imperial Valley motion.

### 3.6.5 Reinforcement Strains

Time histories of tensile strain in reinforcement layer at different elevations in Test 1 are shown in Figure 3.19, Figure 3.20, Figure 3.21, Figure 3.22, and Figure 3.23. Despite of the initial reinforcement strain values, the simulated tensile strains are in reasonable agreement with the measured strains with respect to trends.

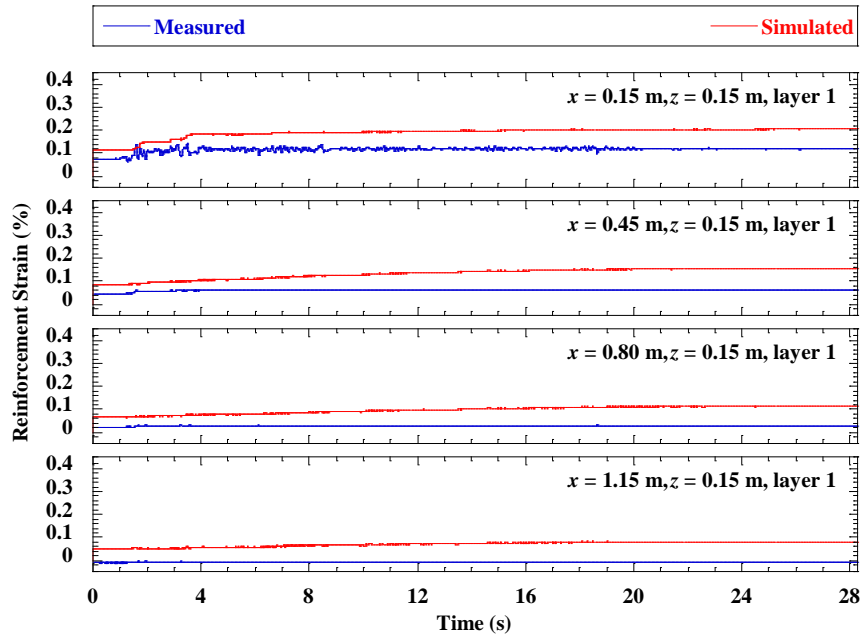


Figure 3.19 Time histories of reinforcement tensile strain in layer 1 for Test 1 during the Imperial Valley motion.

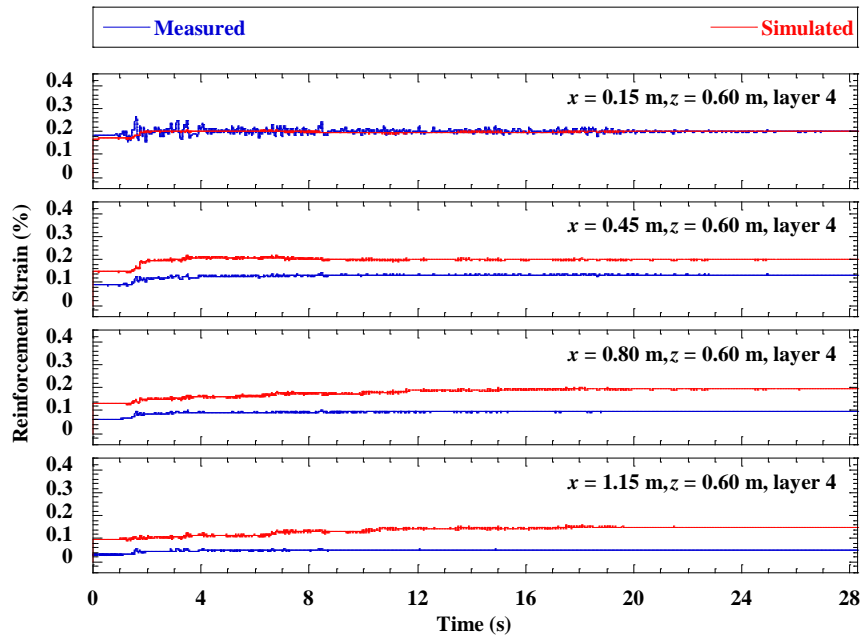


Figure 3.20 Time histories of reinforcement tensile strain in layer 4 for Test 1 during the Imperial Valley motion.

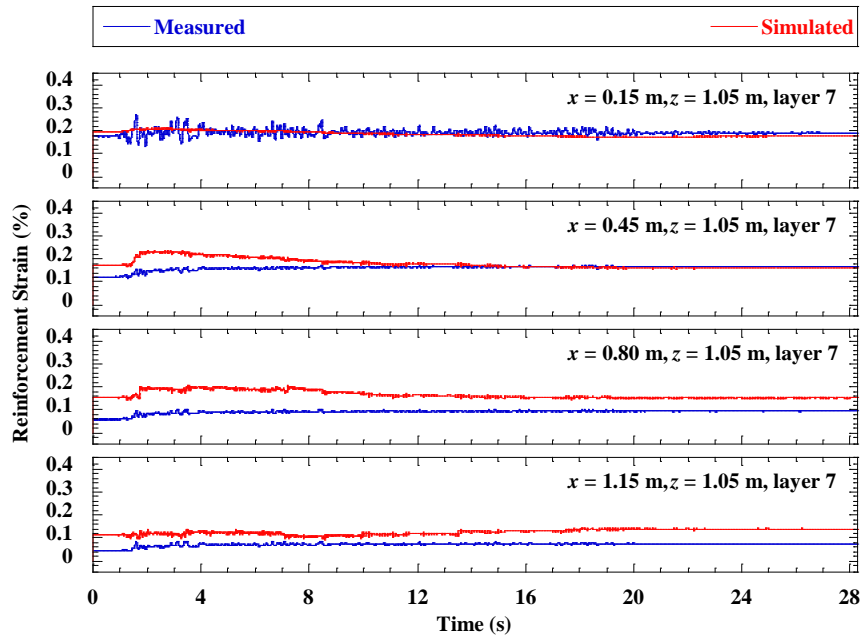


Figure 3.21 Time histories of reinforcement tensile strain in layer 7 for Test 1 during the Imperial Valley motion.

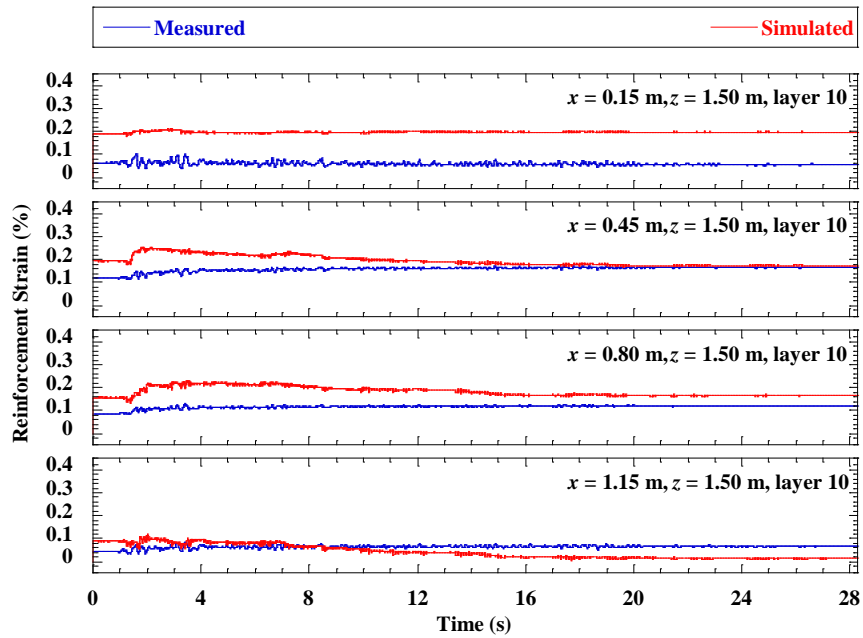


Figure 3.22 Time histories of reinforcement tensile strain in layer 10 for Test 1 during the Imperial Valley motion.

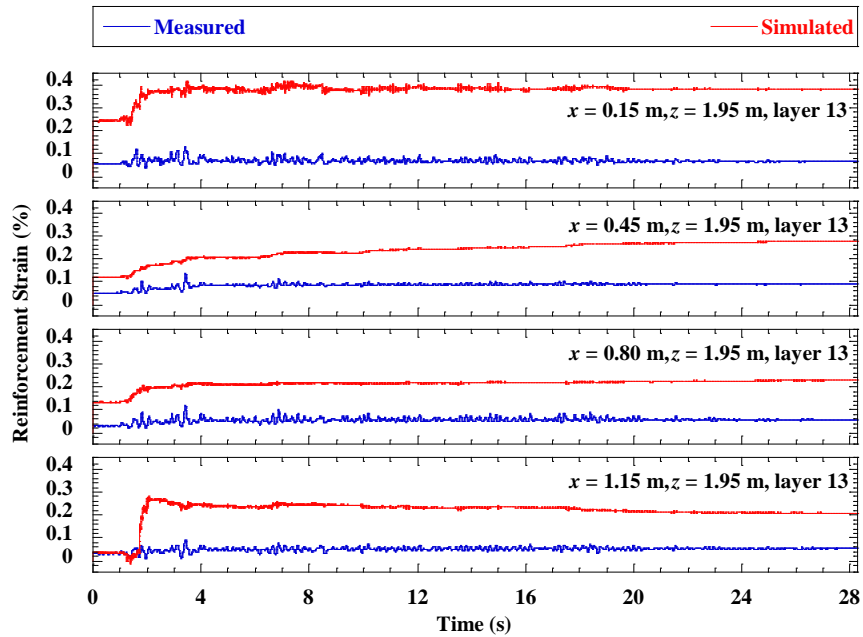


Figure 3.23 Time histories of reinforcement tensile strain in layer 13 for Test 1 during the Imperial Valley motion.

## Chapter 4 Parametric Study of MSE Bridge Abutments under Dynamic Loading

This chapter presents a parametric study on the response of MSE bridge abutments under dynamic loading. Each simulation case was conducted for a single-span full bridge system, including the bridge beam, two MSE abutments, and foundation soil. The variables investigated were reinforcement spacing, reinforcement stiffness, secondary reinforcement, bridge surcharge stress, bridge seat setback distance, bearing pad friction coefficient, and earthquake motion. A baseline case is first described and was used as a point of departure for the remaining simulations. For each series of simulations, only the variable of interest was changed while the other variables were held constant and equal to those for the baseline case.

### 4.1 Baseline Case

#### 4.1.1 Numerical Model

The geometry of the baseline case model for the right-hand side is shown in Figure 4.1, shown for simplicity as the left-hand side is identical. The model represents a single-span bridge system with span  $L_b = 30$  m and symmetrical structures on both ends, resting on foundation soil with a depth of 1 m. Each end structure consists of a lower MSE wall, bridge seat, and upper wall. The lower MSE wall has height  $h = 5$  m and 25 modular facing blocks with dimensions of 0.3 m (length)  $\times$  0.2 m (height). An L-shaped bridge seat with a section thickness of 0.4 m rests on top of the lower MSE wall and has setback distance  $a_b = 0.2$  m from the wall facing. The clear distance between the top facing block and bridge beam  $d_e$  is equal to the bridge seat thickness (0.4 m). The clearance height for the bridge beam above the foundation soil is 5.4 m, which satisfies the FHWA minimum requirement of 4.9 m for interstate highways (Stein and Neuman 2007). The bridge seat has upper surface contact length  $L_c = 1.0$  m with the bridge beam and lower surface contact length  $L_s = 1.5$  m with the soil. There is a 100 mm-wide vertical seismic joint between the bridge beam and bridge seat. Assuming a ratio of bridge beam span to depth  $R_{sd} = L_b/D = 20$ , the depth of the bridge beam  $D = 1.5$  m. A 1.9 m-high upper wall lies behind the bridge seat. The reinforcement has uniform length  $L_r = 3.5$  m ( $0.7h$ ) and vertical spacing  $S_v = 0.2$  m for both the lower MSE wall and upper wall. No secondary (i.e., bearing bed) reinforcement layers are included under the bridge seat for the baseline case. To minimize the influence of boundary conditions on system response, the lateral boundaries are located at a distance of 30 m ( $6h$ ) from the wall facing on each end. Vertical coordinate  $z$  is measured upward from the top surface of the foundation soil.

The soil for the parametric study was the same sand as used for the shaking table tests described in Section 3.3.1, except the relative density was increased to 85%, which satisfies the compaction requirement for typical field MSE walls and abutments. The geogrid reinforcement had a reinforcement stiffness  $J = 1000 \text{ kN/m}$ . The bridge beam had an equivalent unit weight of  $13.33 \text{ kN/m}^3$  to produce an average vertical stress  $\sigma_v = 200 \text{ kPa}$  on the lower MSE wall. Various interfaces between the soil, geogrid, facing block, bridge seat, and bridge beam were included.

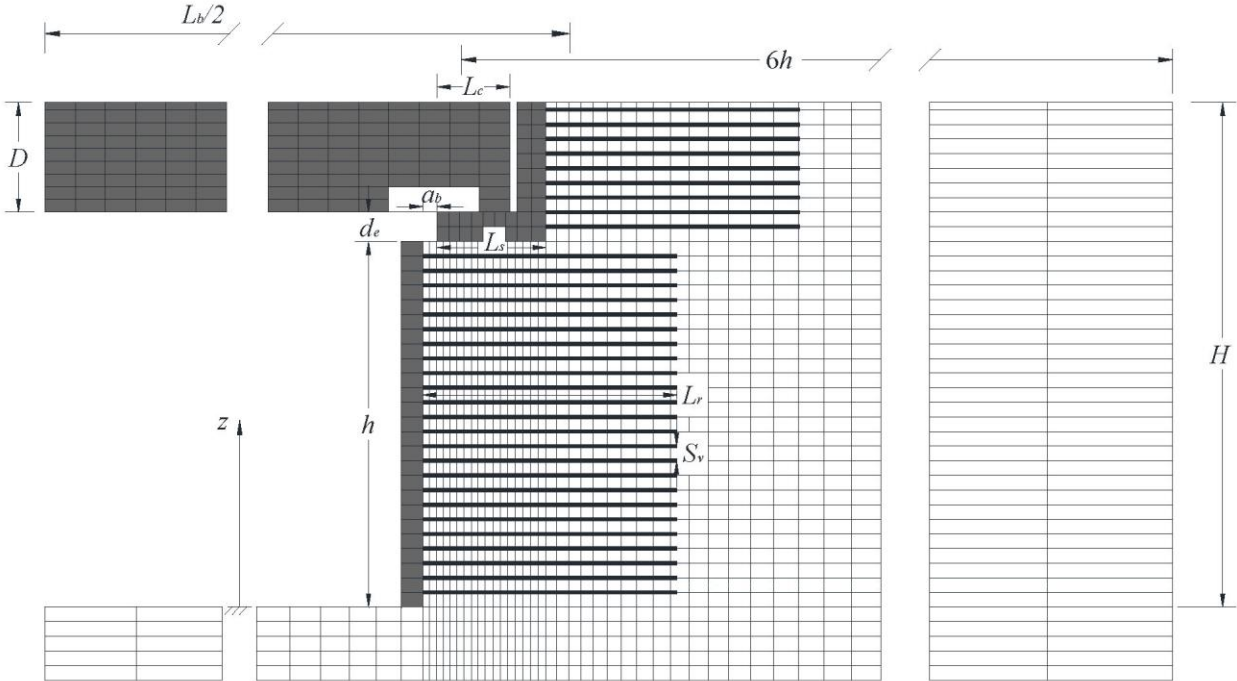


Figure 4.1 Model geometry of baseline case for the right-hand side of the MSE bridge abutment.

For the static analyses, the numerical model was constructed in stages using the modeling approach described in Section 3.4. For the dynamic analysis, free-field conditions were applied at the lateral boundaries of the model to prevent seismic waves from reflecting back to the problem domain and absorb energy. The earthquake motion was the original record of the 1940 Imperial Valley motion (El Centro Station). The corresponding acceleration and displacement time histories are shown in Figure 4.2, and indicate a PGA of  $0.31g$  and peak ground displacement (PGD) of  $130.4\text{ mm}$  with a duration of  $40\text{ s}$ . The earthquake motion was applied at the bottom boundary of the model using the acceleration time history. For each simulation case,  $0.8\%$  Rayleigh damping was assumed for the soil, according to the small strain damping ratio  $D_{s,min}$  in Figure 3.3.

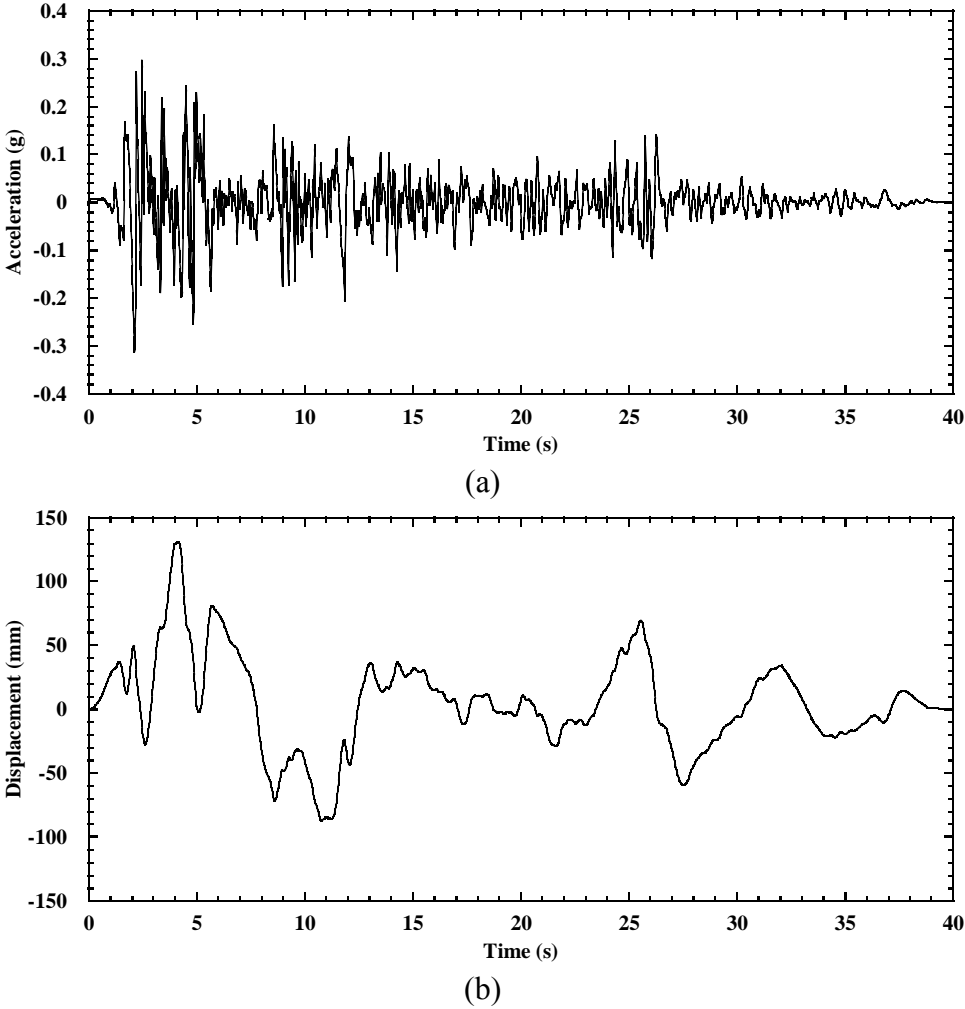


Figure 4.2 Time histories of the 1940 Imperial Valley motion (El Centro Station):  
(a) acceleration; (b) displacement.

### 4.1.2 Simulation Results

The seismic performance of MSE bridge abutments is evaluated in terms of incremental facing displacements, abutment vertical compression, and seismic joint width. The incremental facing displacement is taken relative to the initial facing displacements at the end of construction (i.e., before the start of shaking). The abutment vertical compression is defined as the difference between the average bridge seat settlement and foundation soil settlement.

Time histories of incremental facing displacement at selected elevations for the left and right abutments are shown in Figure 4.3. Results show that the two wall facings moved in-phase during shaking; thus, one facing moved outward as the other facing moved inward. Each wall experienced larger facing displacements at higher elevations and permanent (i.e., residual) deformations by the end of the test. The facing displacements for the right abutment are larger than for the left abutment. The difference of facing displacements between the left and right abutments is attributed to the asymmetry of the earthquake motion with respect to the abutment geometry.

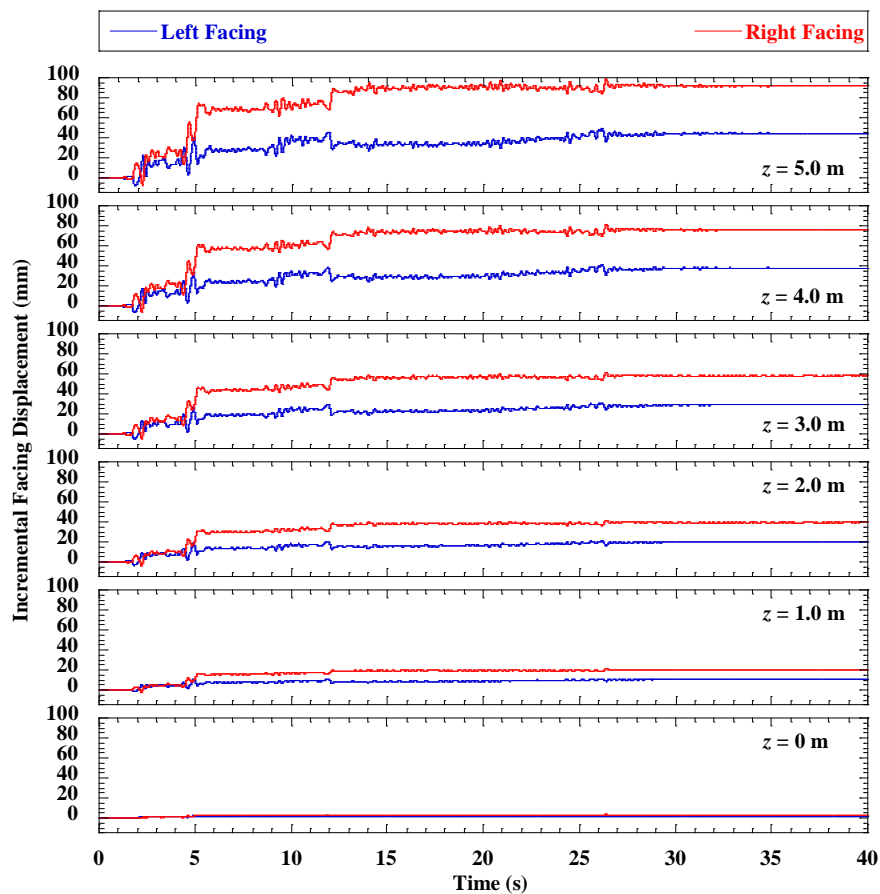


Figure 4.3 Time histories of incremental facing displacements for baseline case.

Profiles of incremental maximum and residual facing displacements for the two abutments are shown in Figure 4.4. The profiles display similar shapes with incremental displacements increasing with elevation and highest values at the top of the wall. The maximum facing displacements for each wall are slightly larger than the residual displacements, which indicates that only a small amount of maximum displacements were recovered at the end of shaking. The maximum incremental residual facing displacements at the top of the wall were 44.4 mm and 92.2 mm for the left and right abutments, respectively.

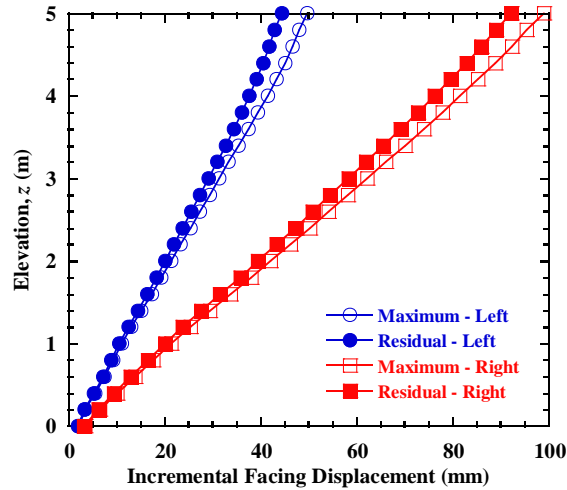


Figure 4.4 Profiles of incremental facing displacements for baseline case.

Time histories of vertical compression for the left and right abutments are shown in Figure 4.5, and indicate similar shapes with respect to both magnitudes and trends. The abutment compressions increased significantly to approximately 4 mm at  $t = 2$  s and to approximately 9 mm at  $t = 5$  s, and then remained nearly constant thereafter. The residual vertical compressions were 9.2 mm and 9.8 mm for the left and right abutments, respectively, corresponding to vertical strains of 0.18% and 0.20% for the 5 m-high lower MSE walls.

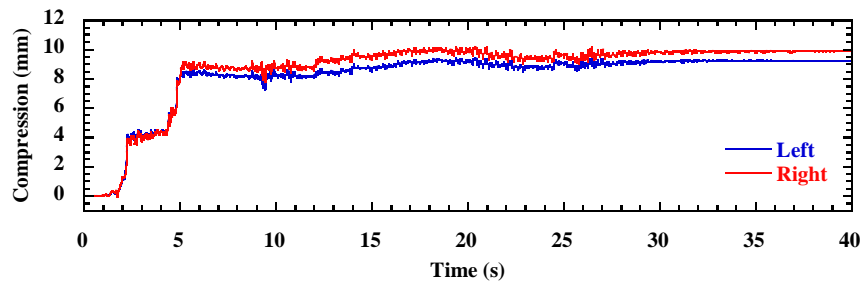


Figure 4.5 Time histories of abutment compression for baseline case.

During shaking, the bridge beam interacted with the MSE abutments through friction developed on the bearing pad interfaces, and the bridge beam may potentially contact the back wall of the bridge seat. Time histories of seismic joint width on either side of the bridge abutment for the baseline case are shown in Figure 4.7. The initial width of seismic joint was 92.5 mm before the shaking event, and then decreased during shaking. The residual widths were 9.1 mm and 50.8 mm after shaking on the left and right ends of the bridge beam, respectively. Both seismic joints decreased in width because of the inward movement of the bridge abutments (i.e., toward the center of the bridge beam). Joint closure did not occur during shaking at either end of the bridge abutment for the baseline case, and thus no impact force between the bridge beam and bridge seat was observed.

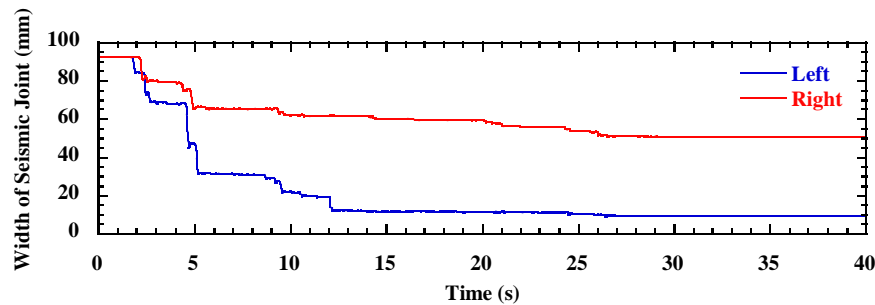
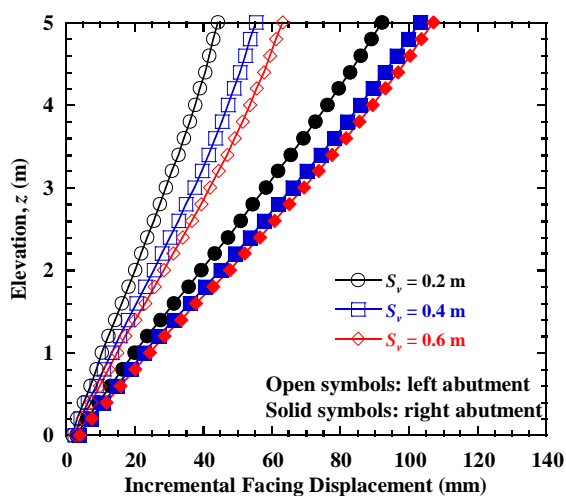


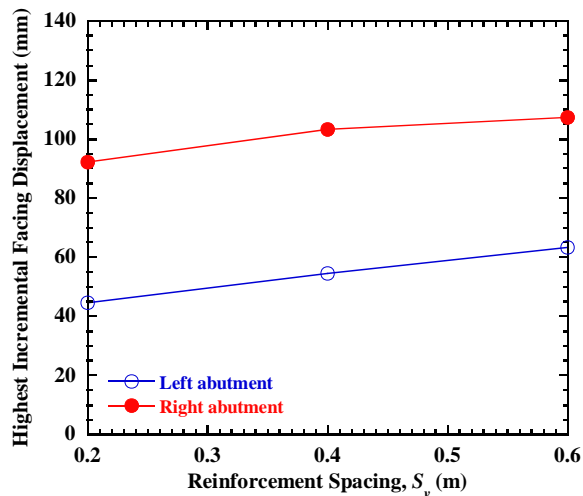
Figure 4.6 Time histories of seismic joint width for baseline case.

#### 4.2 Reinforcement Spacing

Numerical simulations were conducted for reinforcement vertical spacing  $S_v = 0.2$  m, 0.4 m, and 0.6 m for the MSE bridge abutments. Figure 4.7(a) shows the incremental residual facing displacement profiles and indicates consistent trends for the left and right abutments, with facing displacements increasing with increasing reinforcement spacing. The highest facing displacement in Figure 4.7(b) increases almost nearly with increasing reinforcement spacing. Figure 4.8 indicates that reinforcement spacing has significant effects on abutment compression. The average vertical compressions for the left and right abutments are similar for all three cases, with compressions increasing from 9.8 mm to 22.5 mm for the left abutment and from 9.2 mm to 22.2 mm for the right abutment, when  $S_v$  increases from 0.2 m to 0.6 m. The maximum abutment compression of 22.5 mm corresponds to a vertical strain of 0.45% for the 5 m-high lower MSE wall. Time histories for seismic joint width in Figure 4.9 indicate that the widths decrease with increasing reinforcement spacing for both ends. The joint widths were greater than zero during shaking for all cases, which indicated that joint closure did not occur for these cases.



(a)



(b)

Figure 4.7 Effect of reinforcement spacing: (a) residual incremental facing displacement profiles; (b) highest incremental facing displacement.

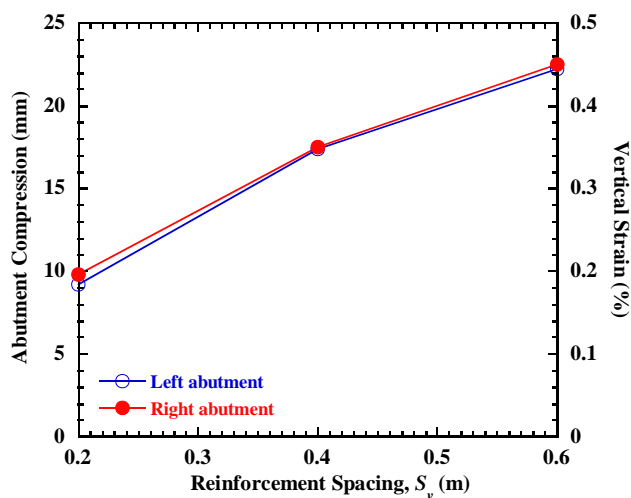


Figure 4.8 Effect of reinforcement spacing on average abutment compression.

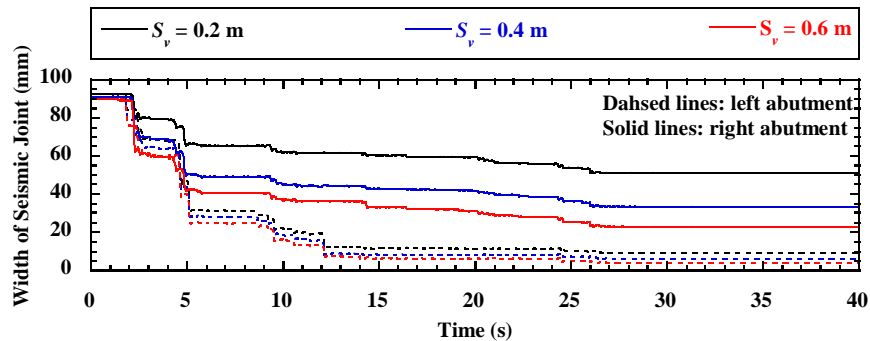


Figure 4.9 Effect of reinforcement spacing on seismic joint width.

### 4.3 Reinforcement Stiffness

Incremental residual facing displacement for reinforcement stiffness  $J = 500, 1000, 1500,$  and  $2000$  kN/m are shown in Figure 4.10. Facing displacements generally increase with increasing reinforcement stiffness. However, the effect becomes relatively small for reinforcement stiffness greater than  $1000$  kN/m. Figure 4.11 indicates that the average abutment compressions decrease significantly with increasing reinforcement stiffness, but the effect becomes less significant with increasing reinforcement stiffness. Figure 4.12 indicates that the widths of seismic joint increase with increasing reinforcement stiffness.

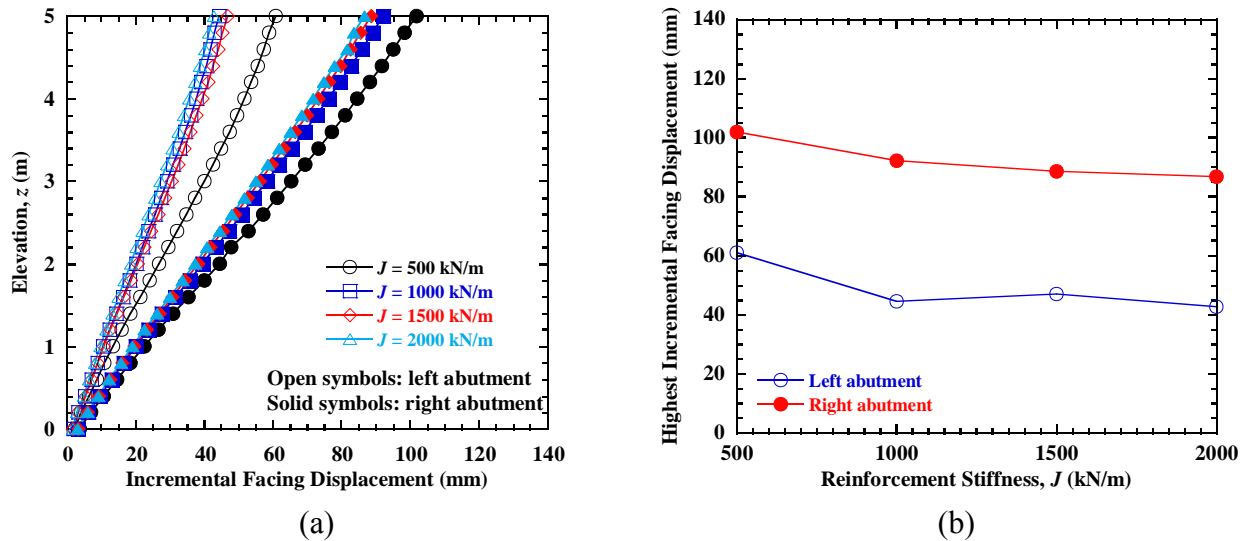


Figure 4.10 Effect of reinforcement stiffness: (a) residual incremental facing displacement profiles; (b) highest incremental facing displacement.

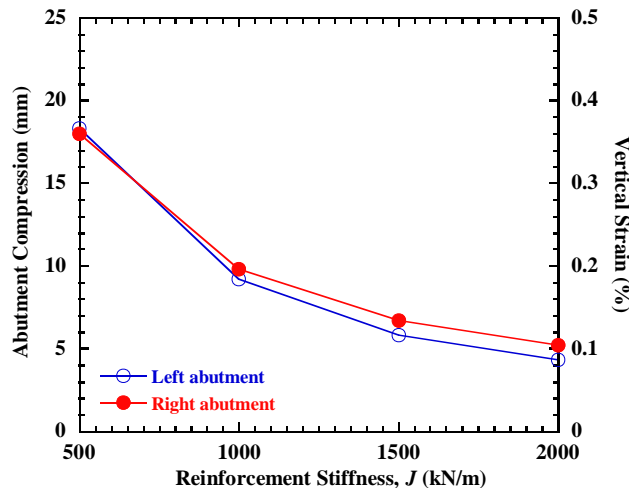


Figure 4.11 Effect of reinforcement stiffness on average abutment compression.

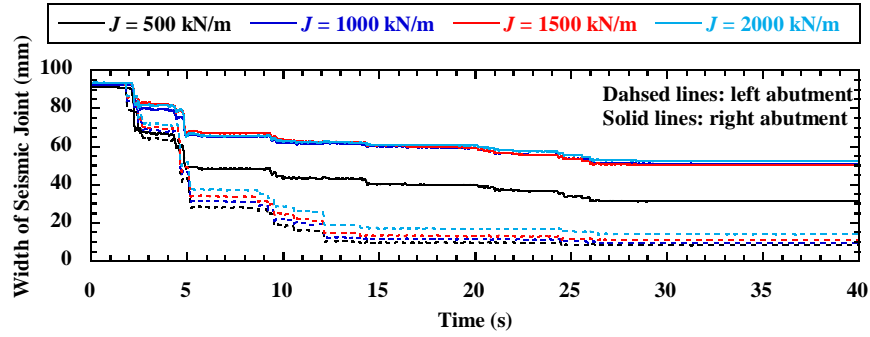


Figure 4.12 Effect of reinforcement stiffness on seismic joint width.

#### 4.4 Secondary Reinforcement

Secondary reinforcement layers are typically included under the bridge seat to provide additional support for the MSE bridge abutments. Simulations were conducted for secondary reinforcement layer number  $n_{sr} = 0, 5, 10,$  and  $15$ . All secondary reinforcement layers had a length of  $1.9 \text{ m}$  ( $L_s + 2a_b$ ) and were not connected to the facing blocks. Figure 4.13 indicates that the secondary reinforcement has a relative small effect on reducing facing displacements under dynamic loading for the conditions investigated. Figure 4.14 shows that the average abutment compressions decrease slightly with increasing secondary reinforcement layers. The widths of seismic joint increase slightly with increasing secondary reinforcement layers, as shown in Figure 4.15.

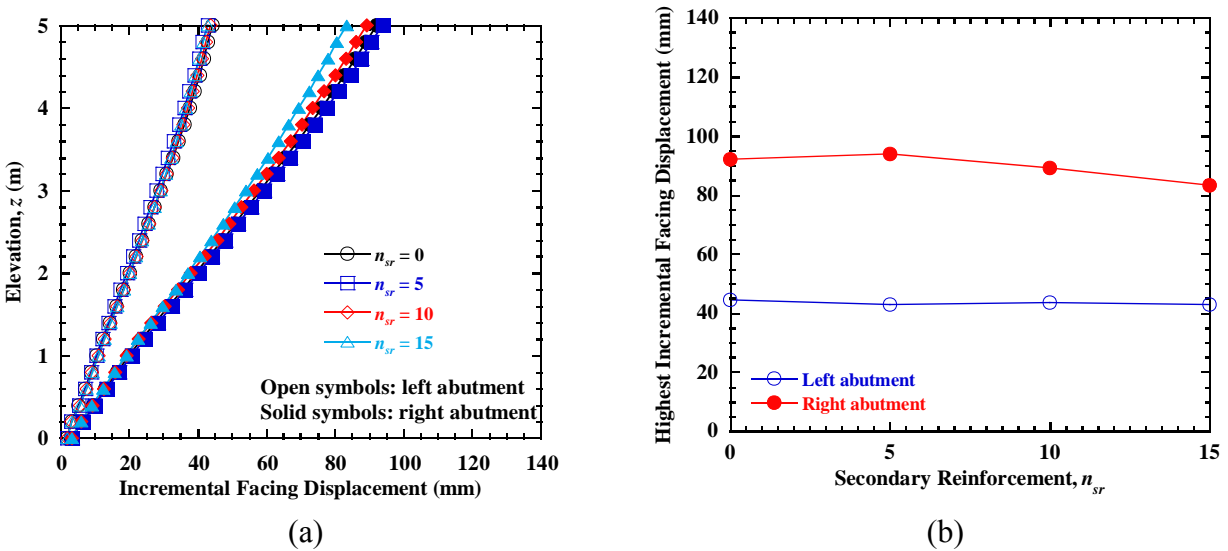


Figure 4.13 Effect of secondary reinforcement: (a) residual incremental facing displacement profiles; (b) highest incremental facing displacement.

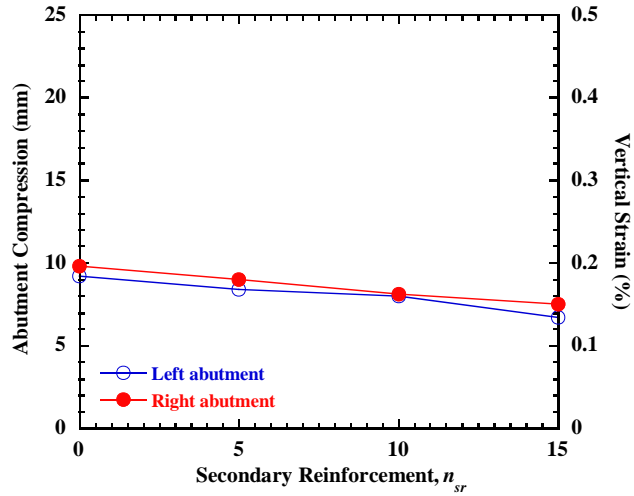


Figure 4.14 Effect of secondary reinforcement on average abutment compression.

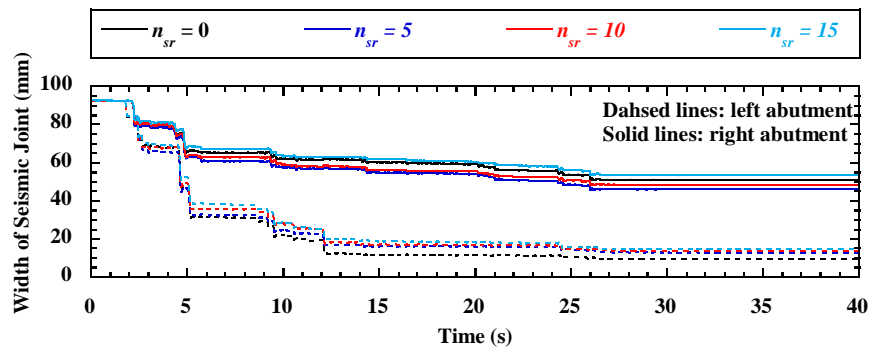


Figure 4.15 Effect of secondary reinforcement on seismic joint width.

### 4.5 Bridge Surcharge Stress

Numerical simulations were conducted for average bridge surcharge stresses on the lower MSE wall of  $\sigma_v = 50, 100, 200,$  and  $400$  kPa. The results in Figure 4.16 indicate that bridge surcharge stress has important effects on facing displacements. The residual facing displacements generally decrease with increasing surcharge stress, which is mainly attributed to the larger soil stiffness associated with greater bridge surcharge stresses. In contrast to the facing displacements, the abutment vertical compressions shown in Figure 4.17 increase with increasing bridge surcharge stress for the conditions investigated, which is different from the experimental results and the simulations of the shaking table tests, possibly because the bridge surcharge stresses were limited to the range of 43 to 66 kPa. The larger mass corresponding to the greater bridge surcharge stress resulted in larger inertial forces during shaking, which may have caused the larger abutment compression. The bridge surcharge stress may have positive or negative effects on abutment compression, which results from the combined effect of change in soil stiffness and inertial forces during shaking, depending on the loading conditions. The seismic joint width is also significantly affected by bridge surcharge stress. The results in Figure 4.18 indicate that residual width is greater for larger bridge surcharge stress. Joint closure occurred on the left end of the bridge beam for  $\sigma_v = 50$  and  $100$  kPa during shaking, and the corresponding peak impact forces are 83 and 57 kN, respectively.

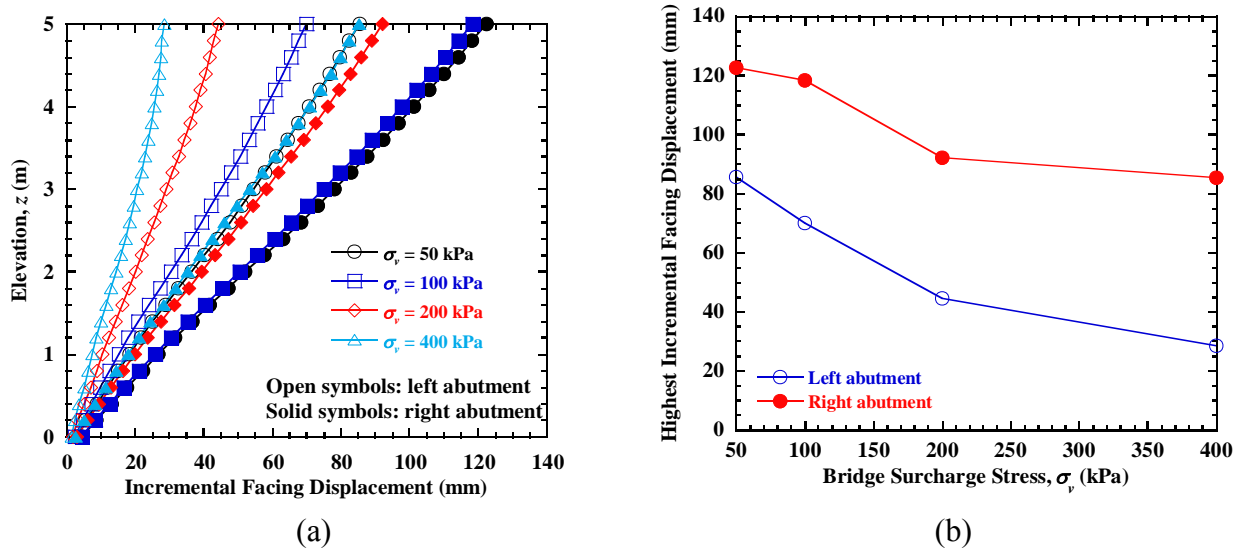


Figure 4.16 Effect of bridge surcharge stress: (a) residual incremental facing displacement profiles; (b) highest incremental facing displacement.

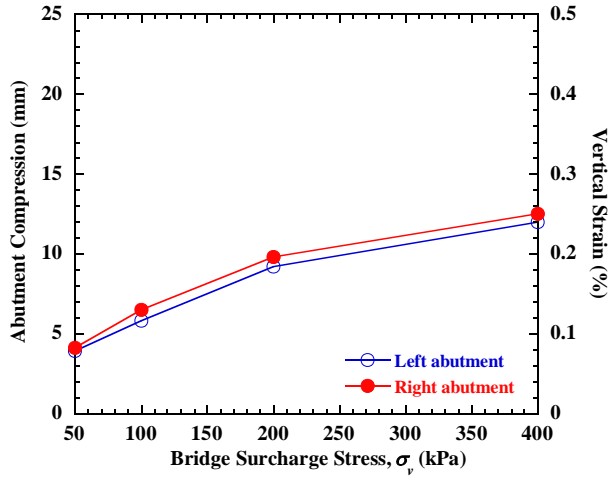


Figure 4.17 Effect of bridge surcharge stress on average abutment compression.

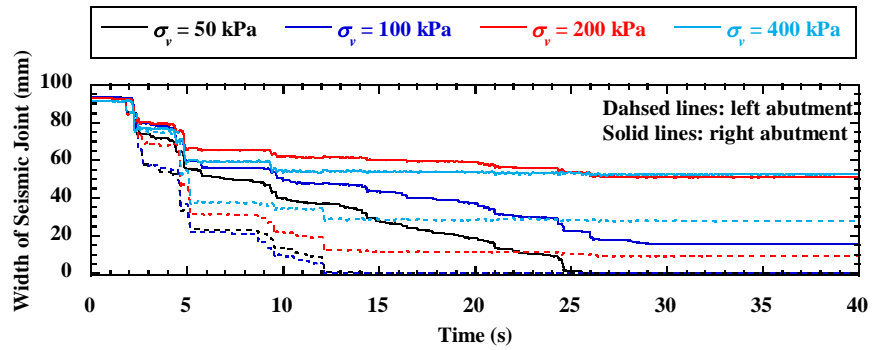


Figure 4.18 Effect of bridge surcharge stress on seismic joint width.

#### 4.6 Bridge Seat Setback Distance

Figure 4.19 shows the incremental residual facing displacements for bridge seat setback distance  $a_b = 0.2, 0.6, 1.0,$  and  $1.4$  m, and indicates that facing displacements generally increase slightly with increasing bridge seat setback distance. Similar to the facing displacements, the abutment vertical compressions in Figure 4.20 also increase with increasing bridge seat setback distance, but the effect becomes negligible for  $a_b > 1.0$  m for the conditions investigated. Joint closure did not occur for all cases, as shown in Figure 4.21.

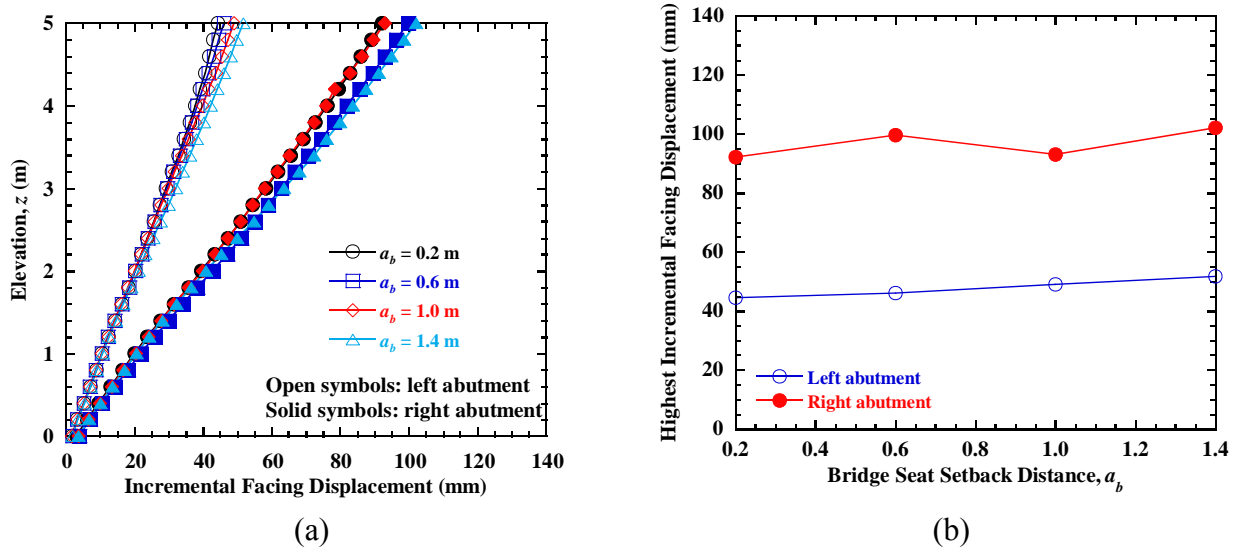


Figure 4.19 Effect of bridge seat setback distance: (a) residual incremental facing displacement profiles; (b) highest incremental facing displacement.

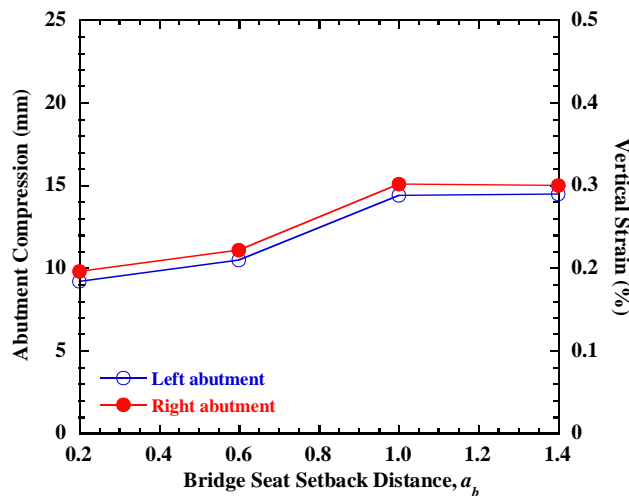


Figure 4.20 Effect of bridge seat setback distance on average abutment compression.

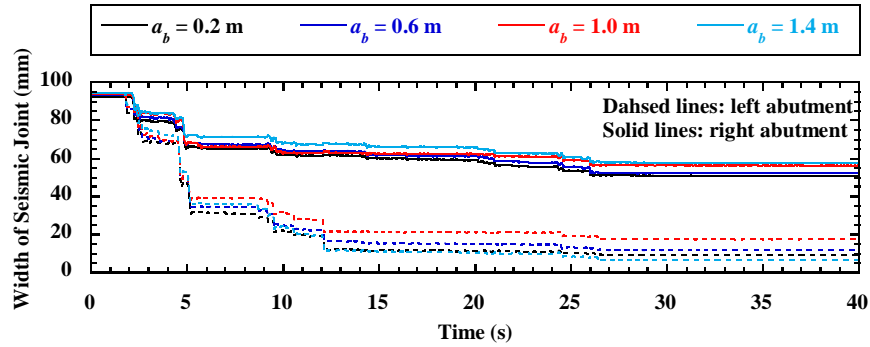


Figure 4.21 Effect of bridge seat setback distance on seismic joint width.

### 4.7 Bearing Pad Friction Coefficient

Numerical simulations were conducted for bridge contact friction coefficient  $\mu = 0.2, 0.4,$  and  $0.6$ . A value of  $0.2$  is conservative,  $0.4$  is suggested by Caltrans for the seismic design of bridge abutments (Caltrans 2007), and  $0.6$  is typical for a concrete-concrete interface. Profiles for incremental residual facing displacements are shown in Figure 4.22(a), and indicate that bearing pad friction coefficient has significant effects on facing displacements under dynamic loading. Larger friction coefficient for bearing pad provided greater restraining forces on the abutment during shaking. The highest facing displacements in Figure 4.22(b) also decrease significantly with increasing bearing pad friction coefficient. Figure 4.23 indicates that the bearing pad friction coefficient has little effects on abutment compression. Time histories for the seismic joint width shown in Figure 4.24 indicate that joint closure occurred for both ends of the abutment for  $\mu = 0.2$ , but not for  $\mu = 0.4$  and  $0.6$ . The peak impact force between the left end of the bridge beam and back wall of the left bridge seat was  $124$  kN.

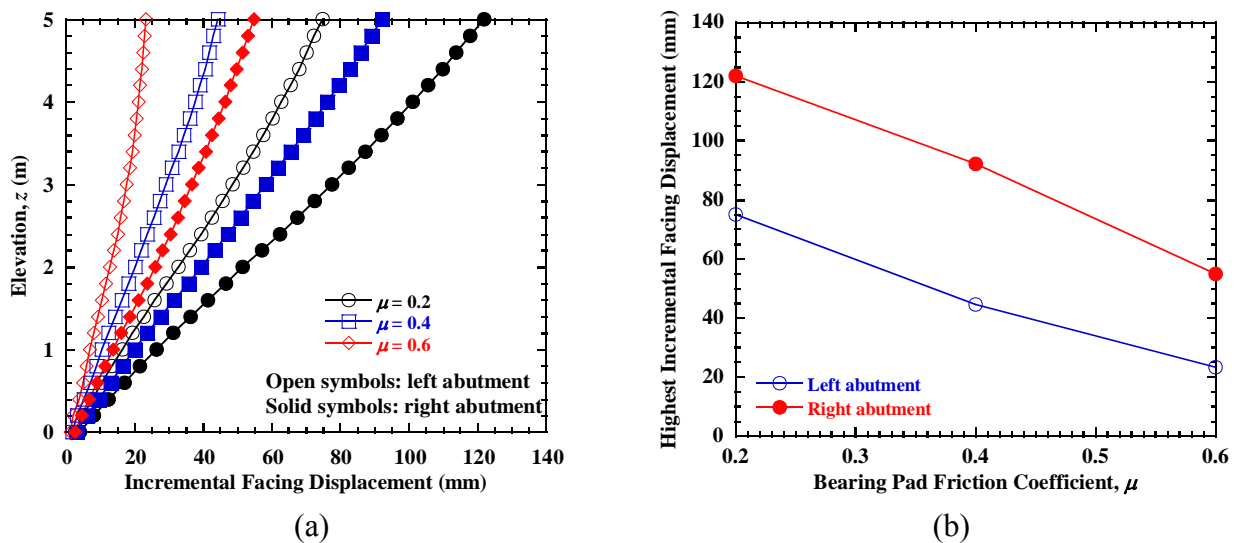


Figure 4.22 Effect of bearing pad friction coefficient: (a) residual incremental facing displacement profiles; (b) highest incremental facing displacement.

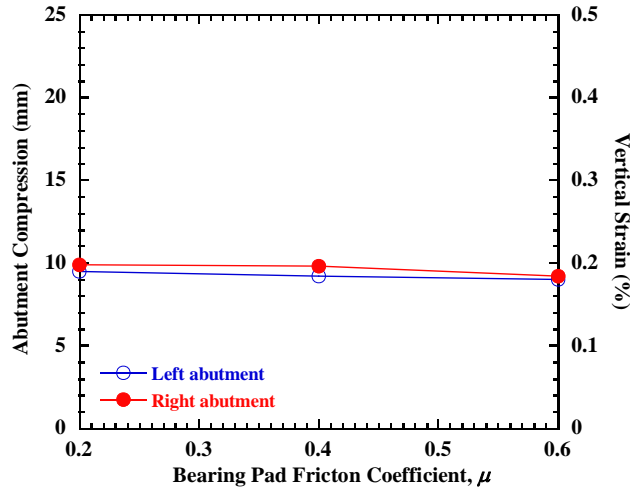


Figure 4.23 Effect of bearing pad friction coefficient on average abutment compression.

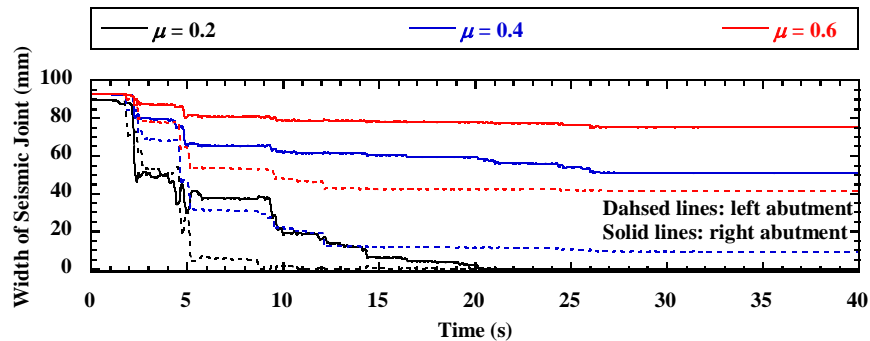
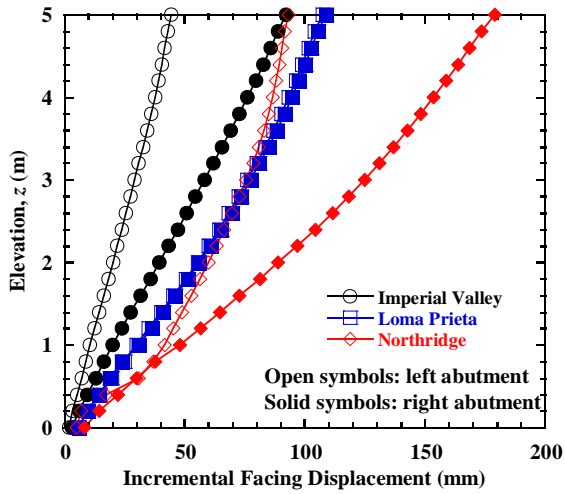


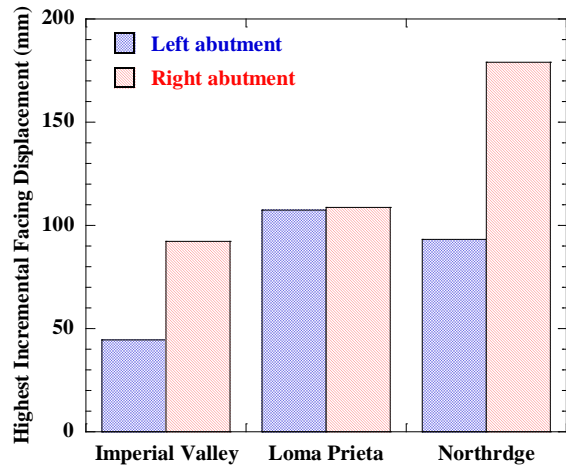
Figure 4.24 Effect of bearing pad friction coefficient on seismic joint width.

#### 4.8 Earthquake Motion

Three different earthquake motions, including the 1940 Imperial Valley motion (El Centro Static, PHA = 0.31g), the 1989 Loma Prieta motion (Capitola Station, PHA = 0.53g), and the 1995 Northridge motion (Newhall station, PHA = 0.58g), were investigated in the parametric study. Profiles of incremental residual facing displacements are shown in Figure 4.25(a), and indicate different shapes for the three earthquake motions. Facing displacements for the left abutment are similar for the Loma Prieta and the Northridge motions, and are larger than for the Imperial Valley motion. Facing displacements of the right abutment for the Northridge motion are larger than for the Imperial Valley and the Loma Prieta motions. The residual abutment compressions for the three earthquake motions are shown in Figure 4.26, and the largest abutment compressions are observed for the Loma Prieta motion. In general, the residual vertical compressions for the left and right abutments are similar for all three motions. Figure 4.27 indicates that joint closure occurred on both ends of the bridge beam for the Loma Prieta and the Northridge motions. The peak impact forces on the left end are 350 and 495 kN, respectively.



(a)



(b)

Figure 4.25 Effect of earthquake motion: (a) residual incremental facing displacement profiles; (b) highest incremental facing displacement.

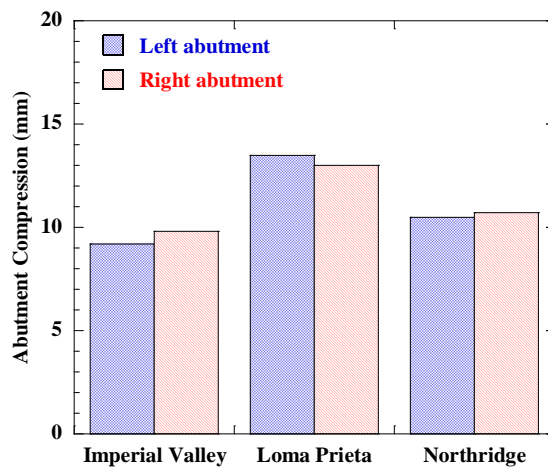


Figure 4.26 Effect of earthquake motion on average abutment compression.

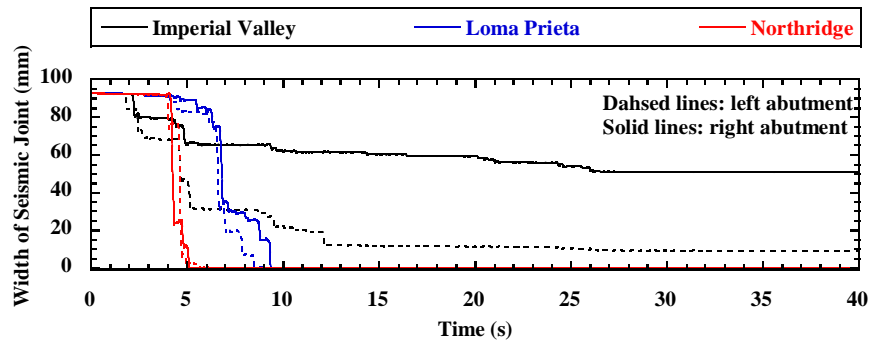


Figure 4.27 Effect of earthquake motion on seismic joint width.

## Chapter 5 Conclusions and Recommendations

### 5.1 Conclusions

Numerical simulations were conducted for shaking table tests on half-scale MSE bridge abutments for shaking in the longitudinal direction. Simulation results were compared with measurements from shaking table tests to validate the numerical model. A parametric study was conducted using the validated numerical model to investigate the effects of various design parameters on the seismic performance of MSE bridge abutments. The following conclusions were reached from this study:

1. A numerical model was developed for the dynamic analysis of MSE bridge abutments. The hysteretic soil model used in this model was observed to capture the reduction in secant modulus with increasing strain, but improvements can be gained in future work by better capturing the volumetric contraction during cyclic loading. The model parameters were calibrated according to modulus reduction curves and damping curves calculated using empirical relationships from published literature.
2. Simulations of the shaking table tests indicated that the numerical model could capture the effects of reinforcement spacing, reinforcement stiffness, and bridge surcharge stress on facing displacements and bridge seat settlements under dynamic loading. Simulated residual facing displacements were overestimated, whereas the simulated residual bridge seat settlements were in good agreement with the measured values.
3. Simulation of a full-scale bridge system with MSE abutments indicate that the two wall facings on both ends of the bridge system moved in-phase during shaking; thus, one facing moved outward as the other facing moved inward. The facing displacements for the right abutment were larger than for the left abutment due to the asymmetry of earthquake motion with respect to the abutment geometry. The maximum incremental residual facing displacements at the top of the wall for a baseline case were 44.4 mm and 92.2 mm for the left and right abutments, respectively.
4. The vertical compressions for a baseline case were similar for the left and right abutments for the Imperial Valley motion. The residual vertical compressions for a baseline case were 9.2 mm and 9.8 mm for the left and right abutments, respectively, corresponding to vertical strains of 0.18% and 0.20% for the 5 m-high lower MSE walls.
5. Joint closure did not occur at either end of the bridge beam for the baseline case, although the joint width decreased on both ends because of the inward movement of the MSE bridge abutments. Accordingly, no impact force was observed between the bridge beam and back wall of the bridge seat during shaking for the baseline case.
6. Results from a parametric study indicate that reinforcement vertical spacing, reinforcement stiffness, and bridge surcharge stress have the most significant effects on facing displacements and abutment compressions for MSE bridge abutments under dynamic loading. Facing displacements and abutment compressions increase with increasing

reinforcement spacing and decreasing reinforcement stiffness. With increasing bridge surcharge stress, facing displacements decrease whereas abutment compressions increase for the conditions investigated, which results from the combined effect of change in soil stiffness and inertial forces during shaking.

7. Secondary reinforcement layers and bridge seat setback distance have relatively small effects on facing displacements and abutment compressions. Bearing pad friction coefficient has significant effects on facing displacements due to restraining forces on the abutment, but little effects on abutment compressions.
8. The shapes of facing displacement profiles are different for different earthquake motions. The residual vertical compressions for the left and ridge abutments are similar for all three earthquake motions investigated. Joint closure occurred for the Loma Prieta and the Northridge motions, and the corresponding peak impact forces on the left end are 350 and 495 kN, respectively.

## **5.2 Recommendations**

The following topics are recommended for future research:

1. The hysteretic soil model can capture the reduction of shear modulus with increasing strain observed in sands. However, it was not able to capture the compression behavior typically observed in sands subjected to cyclic loading. This may have been the reason that the model was not able to capture the facing displacements accurately when simulating the shaking table tests. An improved soil model is needed to better simulate the volumetric behavior under dynamic loading.
2. The numerical model needs to be validated for shaking in other directions to understand the seismic behavior of MSE bridge abutments subjected to shaking in the transverse direction and provide guidance on improving the seismic performance of the side walls of MSE bridge abutments.
3. MSE bridge abutments are 3D structures and will be subjected to shaking in three directions. 3D numerical simulations are needed to investigate the effects of multi-directional shaking on the 3D dynamic response of MSE bridge abutments. Preliminary 3D numerical simulations on static and dynamic response of generic MSE bridge abutments were performed as part of this project and were published in the conference papers by Rong et al. (2017, 2018). However, further research is needed to define appropriate 3D hysteretic constitutive relationships for the backfill soil to improve the reliability of these 3D numerical simulations. The results from the shaking table tests provide useful physical modeling data that can be used for validation of these 3D numerical simulations in the future.

## References

- Abu-Hejleh, N., Zornberg, J.G., Wang, T., and Watcharamonthein, J. (2002). "Monitored displacements of unique geosynthetic-reinforced soil bridge abutments." *Geosynthetics International*, 9(1), 71-95.
- Adams, M., Nicks, J., Stabile, T., Wu, J., Schlatter, W., and Hartmann, J. (2011a). "Geosynthetic reinforced soil integrated bridge system interim implementation guide." *FHWA-HRT-11-026*, U.S. DOT, Washington, D.C.
- Adams, M., Nicks, J., Stabile, T., Wu, J., Schlatter, W., and Hartmann, J. (2011b). "Geosynthetic reinforced soil integrated bridge system synthesis report." *FHWA-HRT-11-027*, U.S. DOT, Washington, D.C.
- Adams, M.T., Schlatter, W., and Stabile, T. (2007). "Geosynthetic-reinforced soil integrated abutments at the Bowman Road Bridge in Defiance County, Ohio." *Geo-Denver 2007*, ASCE, Reston, VA, USA, 1-10.
- Adams, M.T., Schlatter, W., and Stabile, T. (2008). "Geosynthetic-reinforced soil integrated system." *EuroGeo4*, Paper No. 271, Edinburgh, UK.
- Ambauen, S., Leshchinsky, B., Xie, Y., and Rayamajhi, D. (2016). "Service-state behavior of reinforced soil walls supporting spread footings: a parametric study using finite-element analysis." *Geosynthetics International*, 23(3), 156-170.
- Bachus, R.C., Fragaszy, R.J., Jaber, M., Olem, K.L., Yuan, Z., and Jewell, R., (1992). Dynamic response of reinforced soil systems. *USAF Research Report F0 8635-90-C-0198*, 1 & 2, Air Force Civil Engineering Support Agency, Florida, USA.
- Bathurst, R.J., Karpurapu, R.G., and Jarrett, P.M. (1992). "Finite element analysis of a geogrid reinforced soil wall." *ASCE GSP 30: Grouting, Soil Improvement and Geosynthetics*, 2, 1213-1224.
- Bathurst, R.J., and Hatami, K. (1998). "Seismic response analysis of a geosynthetic reinforced soil retaining wall." *Geosynthetics International*, 5(1-2), 127-166.
- Bathurst, R.J., and Hatami, K. (1999). "Numerical study of the influence of base shaking on geosynthetic reinforced retaining walls." *Geosynthetics '99*, Boston, MA, USA, 2, 963-976.
- Bathurst, R.J., and Hatami, K. (2006a). "Parametric analysis of reinforced soil walls with different height and reinforcement stiffness." *8th International Conference on Geosynthetics*, Yokohama, Japan, 1343-1346.
- Bathurst, R.J., and Hatami, K. (2006b). "Physical to computational modelling of reinforced soil walls under static loading." *2nd International Conference on Physical Modeling in Geotechnics*, Hong Kong, China, 1, 3-17.
- Bathurst, R.J., Huang, B., and Hatami, K. (2008). "Numerical modeling of geosynthetic reinforced retaining walls." *12th International Conference of the International Association for Computer Methods and Advances in Geomechanics (IACMAG)*, Goa, India, 4071-4080.

- Bathurst, R.J., Nernheim, A., Walters, D.L., Allen, T.M., Burgess, P., and Saunders, D.D. (2009). "Influence of reinforcement stiffness and compaction on the performance of four geosynthetic reinforced soil walls." *Geosynthetics International*, 16(1), 43-59.
- Berg, R.R., Christopher, B.R., and Samtani, N. (2009). "Design and construction of mechanically stabilized earth walls and reinforced soil slopes – Volume I." *FHWA-NHI-10-024/FHWA GEC 011-Vol I*, U.S. DOT, Washington, D.C.
- Budge, A.S., Dasenbrock, D.D., Mattison, D.J., Bryant, G.K., Grosser, A.T., Adams, M., and Nicks, J. (2014). Instrumentation and early performance of a large grade GRS-IBS wall. *Geo-Congress 2014*, ASCE, Reston, VA, USA, 4213-4227.
- Cai, Z., and Bathurst, R.J. (1995). "Seismic response analysis of geosynthetic reinforced soil segmental retaining walls by finite element method." *Computers and Geotechnics*, 17(4), 523-546.
- Caltrans. (2004). Section 5 - Retaining Walls, *Bridge Design Specifications*, August 2004.
- Caltrans. (2017). Memo to Designers 5-1, March 2017.
- Damians, I.P., Bathurst, R.J., Josa, A., Lloret, A. (2014). "Numerical study of the influence of foundation compressibility and reinforcement stiffness on the behavior of reinforced soil walls." *International Journal of Geotechnical Engineering*, 8(3), 247-259.
- Darendeli, I.S. (2001). Development of a new family of normalized modulus reduction and material damping curves. *Ph.D. Thesis*. University of Texas, Austin.
- Duncan, J.M., Byrne, P., Wong, K.S., and Mabry, P. (1980). Strength, stress-strain and bulk modulus parameters for finite element analysis of stresses and movements in soil masses. *Report No. UCB/GT/80-01*, University of California, Berkeley, CA, USA.
- El-Emam, M., and Bathurst, R.J. (2004). "Experimental design, instrumentation and interpretation of reinforced soil wall response using a shaking table." *International Journal of Physical Modelling in Geotechnics*, 4(4), 13-32.
- El-Emam, M., and Bathurst, R.J. (2005). "Facing contribution to seismic response of reduced-scale reinforced soil walls." *Geosynthetics International*, 12(5), 215-238.
- El-Emam, M., and Bathurst, R.J. (2007). "Influence of reinforcement parameters on the seismic response of reduced-scale reinforced soil retaining walls." *Geotextiles and Geomembranes*, 25(1), 33-49.
- El-Emam, M., Bathurst, R.J., and Hatami, K. (2004). "Numerical modeling of reinforced soil retaining walls subjected to base acceleration." *13th World Conference on Earthquake Engineering*, Vancouver, BC, Canada, Paper No. 2621.
- Fakharian, K., and Attar, I.H. (2007). "Static and seismic numerical modeling of geosynthetic-reinforced soil segmental bridge abutments." *Geosynthetics International*, 14(4), 228-243.
- FLAC2D Version 7.0* [Computer software]. (2011). Itasca Consulting Group, Minneapolis, MN, USA.
- Guler, E., Cicek, E., Demirkan, M.M., Hamderi, M. (2012). "Numerical analysis of reinforced soil walls with granular and cohesive backfills under cyclic loads." *Bulletin of Earthquake Engineering*, 10(3), 793-811.

- Guler, E., Hamderi, M., and Demirkan, M.M. (2007). "Numerical analysis of reinforced soil-retaining wall structures with cohesive and granular backfills." *Geosynthetics International*, 14(6), 330–345.
- Hatami, K., and Bathurst, R.J. (2000a). "Effect of structural design on fundamental frequency of reinforced-soil retaining walls." *Soil Dynamics and Earthquake Engineering*, 19(3), 137-157.
- Hatami, K., and Bathurst, R.J. (2000b). "Investigation of seismic response of reinforced soil retaining walls." *4th International Conference on Recent Advances in Geotechnical Earthquake Engineering and Soil Dynamics*, San Diego, CA, USA, Paper No. 7.18.
- Hatami, K., and Bathurst, R.J. (2005a). "Development and verification of a numerical model for the analysis of geosynthetic reinforced soil segmental walls under working stress conditions." *Canadian Geotechnical Journal*, 42(4), 1066-1085.
- Hatami, K., and Bathurst, R.J. (2005b). "Verification of a numerical model for reinforced soil segmental retaining walls." *GeoFrontiers 2005: Slopes and Retaining Structures under Seismic and Static Conditions*, Austin, Texas, USA.
- Hatami, K., and Bathurst, R.J. (2005c). "Parametric analysis of reinforced soil walls with different backfill material properties." *North American Geosynthetics Society 2005 Conference*, Las Vegas, Nevada, USA.
- Hatami, K., and Bathurst, R.J. (2006). "Numerical model for reinforced soil segmental walls under surcharge loading." *Journal of Geotechnical and Geoenvironmental Engineering*, 132(6), 673-684.
- Helwany, S.M.B., Budhu, M., and McCallen, D. (2001). "Seismic analysis of segmental retaining walls. I: Effects of facing details." *Journal of Geotechnical and Geoenvironmental Engineering*, 127(9), 750-756.
- Helwany, S.M.B., and McCallen, D. (2001). "Seismic analysis of segmental retaining walls. II: Model verification." *Journal of Geotechnical and Geoenvironmental Engineering*, 127(9), 741-749.
- Helwany, S.M.B., Reardon, G., and Wu, J.T.H. (1999). "Effects of backfill on the performance of GRS retaining walls." *Geotextiles and Geomembranes*, 17, 1-16.
- Helwany, S.M.B., Wu, J.T.H., and Froessl, B. (2003). "GRS bridge abutments – an effective means to alleviate bridge approach settlement." *Geotextiles and Geomembranes*, 21, 177-196.
- Helwany, S.M.B., Wu, J.T.H., and Kitsabunnarat, A. (2007). "Simulating the behavior of GRS bridge abutments." *Journal of Geotechnical and Geoenvironmental Engineering*, 133(10), 1129-1240.
- Helwany, S.M.B., Wu, J.T.H., and Meinholz, P. (2012). Seismic design of geosynthetic-reinforced soil bridge abutments with modular block facing. *NCHRP Web-Only Document 187*, Transportation Research Board, Washington, D.C.
- Ho, S.K., and Rowe, R.K. (1997). "Effect of wall geometry on the behaviour of reinforced soil walls." *Geotextiles and Geomembranes*, 14(10), 521-541.

- Huang, B., Bathurst, R.J., and Hatami, K. (2009). "Numerical study of reinforced soil segmental walls using three different constitutive soil models." *Journal of Geotechnical and Geoenvironmental Engineering*, 135(10), 1486-1498.
- Huang, B., Bathurst, R.J., Hatami, K., and Allen, T.M. (2010). "Influence of toe restraint on reinforced soil segmental walls." *Canadian Geotechnical Journal*, 47(8), 885-904.
- Karpurapu, R.G., and Bathurst, R.J. (1995). "Behaviour of geosynthetic reinforced soil retaining walls using the finite element method." *Computers and Geotechnics*, 17(3), 279-299.
- Lee, K.Z.Z., and Chang, N.Y. (2012). "Predictive modeling on seismic performances of geosynthetic-reinforced soil walls." *Geotextiles and Geomembranes*, 35, 25-40.
- Lee, K.Z.Z., Chang, N.Y., and Ko, H.Y. (2010). "Numerical simulation of geosynthetic-reinforced soil walls under seismic shaking." *Geotextiles and Geomembranes*, 28, 317-334.
- Lee, W. (2000). "Internal stability of analyses of geosynthetic reinforced retaining walls." *Ph.D. Thesis*, University of Washington, Seattle, USA.
- Lee, K.Z.Z., and Wu, J.T.H. (2004). "A synthesis of case histories on GRS bridge-supporting structures with flexible facing." *Geotextiles and Geomembranes*, 22(4), 181-204.
- Leshchinsky, B. (2014). "Limit analysis optimization of design factors for mechanically stabilized earth wall-supported seats." *Transportation Infrastructure Geotechnology*, 1(2), 111-128.
- Leshchinsky, D, and Vulova, C. (2001). "Numerical investigation of the effects of geosynthetic spacing on failure mechanisms in MSE block walls." *Geosynthetics International*, 8(4), 343-365.
- Ling, H.I. (2003). "Finite element applications to reinforced soil retaining walls – simplistic versus sophisticated analyses." *ASCE GSP 143: Geomechanics: Testing, Modeling and Simulation*, 217-236.
- Ling, H.I., Cardany, C., Sun, L-X., and Hashimoto, H. (2000). "Finite element analysis of a geosynthetic-reinforced soil retaining wall with concrete-block facing." *Geosynthetics International*, 7(2), 137-162.
- Ling, H.I., and Leshchinsky, D. (2003). "Finite element parametric studies of the behavior of segmental block reinforced soil retaining walls." *Geosynthetics International*, 10(3), 77-94.
- Ling, H.I., Liu, H., Kaliakin, V., and Leshchinsky, D. (2004). "Analyzing dynamic behavior of geosynthetic-reinforced soil retaining walls." *Journal of Engineering Mechanics*, 130(8), 911-920.
- Ling, H.I., Mohri, Y., Leshchinsky, D., Burke, C., Matsushima, K., and Liu, H. (2005a). "Large scale shaking table tests on modular block reinforced soil retaining wall." *Journal of Geotechnical and Geoenvironmental Engineering*, 131(4), 465-476.
- Ling, H.I., Liu, H., and Mohri, Y. (2005b). "Parametric studies on the behavior of reinforced soil retaining walls under earthquake loading." *Journal of Engineering Mechanics*, 131(10), 1056-1065.

- Ling, H.I., Yang, S., Leshchinsky, D., Liu, H., and Burke, C. (2010). "Finite-element simulations of full-scale modular-block reinforced soil retaining walls under earthquake loading." *Journal of Engineering Mechanics*, 136(5), 653-661.
- Menq, F. (2003). Dynamic properties of sandy and gravelly soils. *Ph.D. Thesis*. University of Texas, Austin.
- Mirmoradi, S.H., and Ehrlich, M. (2015). "Numerical evaluation of the behavior of GRS walls with segmental block facing under working stress conditions." *Journal of Geotechnical and Geoenvironmental Engineering*, 141(3), 04014109.
- Mirmoradi, S.H., and Ehrlich, M., (2017). "Effects of facing, reinforcement stiffness, toe resistance, and height on reinforced walls." *Geotextiles and Geomembranes*, 45(1), 67-76.
- Ren, F., Zhang, F., Xu, C., Wang, G. (2016). "Seismic evaluation of reinforced-soil segmental retaining walls." *Geotextiles and Geomembranes*, 44(4), 604-614.
- Rong, W., Zheng, Y., McCartney, J.S., and Fox, P.J. (2017). "3D deformation behavior of a geosynthetic reinforced soil bridge abutment." *Geotechnical Frontiers 2017*. Orlando, FL. ASCE. 44-55.
- Rong, W., Zheng, Y., McCartney, J.S., Fox, P.J. (2018). "Seismic-induced deformations of a geosynthetic reinforced soil bridge abutment subjected to longitudinal shaking. IFCEE 2018. Orlando, FL. Mar. 6-10. 147-157.
- Rowe, R.K., and Ho, S.K. (1997). "Continuous panel reinforced soil walls on rigid foundations." *Journal of Geotechnical and Geoenvironmental Engineering*, 123(10), 912-920.
- Rowe, R.K., and Ho, S.K. (1998). "Horizontal deformation in reinforced soil walls." *Canadian Geotechnical Journal*, 35(2), 312-327.
- Saghebfar, M., Abu-Farsakh, M., Ardah, A., and Chen, Q. (2017). Performance monitoring of Geosynthetic Reinforced Soil Integrated Bridge System (GRS-IBS) in Louisiana." *Geotextiles and Geomembranes*, 45(2), 34-47.
- Segrestin, P., and Bastick, M. (1988). "Seismic design of reinforced earth retaining wall – the contribution of finite element analysis." *International Geotechnical Symposium on Theory and Practice of Earth Reinforcement*, Fukuoka, Kyushu, Japan, 577-582.
- Skinner, G.D., and Rowe, R.K. (2005). "Design and behavior of a geosynthetic reinforced retaining wall and bridge abutment on a yielding foundation." *Geotextiles and Geomembranes*, 23, 234-260.
- Warren, K.A., Schlatter, W., Adams, M., Stabile, T., and LeGrand, D. (2010). Preliminary results for a GRS Integrated Bridge System supporting a large single span bridge. *2010 Earth Retention Conference*, ASCE, Reston, VA, USA, 612-619.
- Won, G.W., Hull, T., and De Ambrosis, L. (1996). "Performance of a geosynthetic segmental block wall structure to support bridge abutments." *Earth Reinforcement*, Vol. 1, Balkema, Rotterdam, Netherlands, 543–548.
- Wu, J.T.H., Lee, K.Z.Z, Helwany, S.B., and Ketchart, K. (2006a). Design and construction guidelines for geosynthetic-reinforced soil bridge abutments with a flexible facing. *NCHRP Report 556*, Transportation Research Board, Washington, DC.

- Wu, J.T.H., Lee, K.Z.Z, and Pham, T. (2006b). "Allowable bearing pressures of bridge sills on GRS abutments with flexible facing." *Journal of Geotechnical and Geoenvironmental Engineering*, 132(7), 830-841.
- Xie, Y., and Leshchinsky, B. (2015). "MSE walls as bridge abutments: Optimal reinforcement density." *Geotextiles and Geomembranes*, 43(2), 128-138.
- Yen, W.-H.P., Chen, G., Buckle, I., Allen, T., Alzamora, D., Ger, J., and Arias, J.G. (2011). Post-earthquake reconnaissance report on transportation infrastructure: Impact of the February 27, 2010, offshore Maule Earthquake in Chile, *FHWA-HRT-11-030*, U.S. DOT, Washington, D.C.
- Yogendrakumar, M., and Bathurst, R.J. (1992). "Numerical simulation of reinforced soil structures during blast loadings." *Transportation Research Record 1336*, 1-8.
- Yogendrakumar, M., Bathurst, R.J., and Finn, W.D.L. (1991). "Response of reinforced soil walls to earthquake loads." *IX Panamerican Conference on Soil Mechanics and Foundation Engineering*, Vina del Mar, Chile, 659-672.
- Yogendrakumar, M., Bathurst, R.J. and Finn, W.D.L. (1992). "Dynamic response analysis of a reinforced soil retaining wall." *Journal of Geotechnical Engineering*, 118(8), 1158-1167.
- Yu, Y., Bathurst, R.J., and Allen, T.M. (2016). "Numerical modeling of the SR-18 geogrid reinforced modular block retaining walls." *Journal of Geotechnical and Geoenvironmental Engineering*, 10.1061/(ASCE)GT.1943-5606.0001438, 04016003.
- Zevgolis, I, and Bourdeau, P.L. (2007). Mechanically stabilized earth wall abutments for bridge support. *FHWA/IN/JTRP-2006/38*, Indiana Department of Transportation and Purdue University, West Lafayette, IN.
- Zheng, Y., and Fox, P.J. (2016). "Numerical investigation of geosynthetic-reinforced soil bridge abutments under static loading." *Journal of Geotechnical and Geoenvironmental Engineering*, 10.1061/(ASCE)GT.1943-5606.0001452, 04016004.
- Zheng, Y., and Fox, P.J. (2017). "Numerical investigation of the geosynthetic reinforced soil-integrated bridge system under static loading." *Journal of Geotechnical and Geoenvironmental Engineering*, 10.1061/(ASCE)GT.1943-5606.0001665, 04017008.